Global three-dimensional MHD simulation of a space weather event: CME formation, interplanetary propagation, and interaction with the magnetosphere

Clinton P. T. Groth,[1] Darren L. De Zeeuw, and Tamas I. Gombosi

Space Physics Research Laboratory, Department of Atmospheric, Oceanic and Space Sciences
University of Michigan, Ann Arbor

Kenneth G. Powell

W. M. Keck Foundation Laboratory for Computational Fluid Dynamics, Department of Aerospace
Enginnering
University of Michigan, Ann Arbor

Abstract. A parallel adaptive mesh refinement (AMR) finite-volume scheme for predicting ideal MHD flows is used to simulate the initiation, structure, and evolution of a coronal mass ejection (CME) and its interaction with the magnetosphere-ionosphere system. The simulated CME is driven by a local plasma density enhancement on the solar surface with the background initial state of the corona and solar wind represented by a newly devised "steady state" solution. The initial solution has been constructed to provide a reasonable description of the time-averaged solar wind for conditions near solar minimum: (1) the computed magnetic field near the Sun possesses high-latitude polar coronal holes, closed magnetic field flux tubes at low latitudes, and a helmet streamer structure with a neutral line and current sheet; (2) the Archimedean spiral topology of the interplanetary magnetic field is reproduced; (3) the observed two-state nature of the solar wind is also reproduced with the simulation yielding fast and slow solar wind streams at high and low latitudes, respectively; and (4) the predicted solar wind plasma properties at 1 AU are consistent with observations. Starting with the generation of a CME at the Sun, the simulation follows the evolution of the solar wind disturbance as it evolves into a magnetic cloud and travels through interplanetary space and subsequently interacts with the terrestrial magnetosphere-ionosphere system. The density-driven CME exhibits a two-step release process, with the front of the CME rapidly accelerating following the disruption of the near-Sun closed magnetic field line structure and then moving at a nearly constant speed of $\sim$560 km/s through interplanetary space. The CME also produces a large magnetic cloud ($> 100 \, R_s$ across) characterized by a magnetic field that smoothly rotates northward and then back again over a period of $\sim$2 days at 1 AU. The cloud does not contain a sustained period with a strong southward component of the magnetic field, and, as a consequence, the simulated CME is somewhat ineffective in generating strong geo-magnetic activity at Earth. Nevertheless, the simulation results illustrate the potential, as well as current limitations, of the MHD-based space weather model for enhancing the understanding of coronal physics, solar wind plasma processes, magnetospheric physics, and space weather phenomena. Such models will provide the foundation for future, more comprehensive space weather prediction tools.

1. Introduction

Space weather is of growing importance to the scientific community and refers to conditions at a particular place and time on the Sun and in the solar wind, magnetosphere, ionosphere, and thermosphere that can influence the performance and reliability of spaceborne and ground-based technological systems and can affect human life or health. It has been established that adverse conditions in the space environment can cause disruption of satellite operations, communications, navigation, and electric power distribution grids, thereby leading to broad socioeconomic losses [*Wright*, 1997]. These influences on the geospace environment have prompted renewed efforts to enhance our understanding of space weather and develop effective tools for space weather prediction.

Global computational models based on first principles descriptions of the physics represent a very important component of efforts to understand space plasma phenomena associated with space weather, including the large-scale solar corona, the solar wind, the solar wind interaction with planetary magnetospheres, and the initiation, structure, and evolution of solar wind disturbances. Presently, and in the foreseeable future, numerical models based on the equations of magnetohydrodynamics (MHD) are the only self-consistent mathematical descriptions that can span the enormous distances associated with large-scale space weather phenomena. Although providing only a relatively low-order approximation to the actual behavior of plasmas (i.e., ideal MHD models neglect kinetic effects, ignore resistivity and diffusion, and treat ions and electrons as a single fluid), MHD models have been used successfully to simulate many important space plasma processes and provide a powerful means for significantly advancing the understanding of such processes.

Global MHD simulations have been used for a long time to simulate the global magnetospheric configuration and to investigate the response of the magnetosphere-ionosphere system to changing solar wind conditions. The first global-scale three-dimensional (3-D) MHD simulations of the solar wind–magnetosphere system were published in the early 1980s [*LeBoeuf et al.*, 1981; *Wu et al.*, 1981; *Brecht et al.*, 1981, 1982]. Since then, MHD models have been used to study a range of processes, including the global magnetic field configuration, reconnection in the tail and at the dayside magnetopause, the dependence of magnetospheric convection on the orientation of the interplanetary magnetic field (IMF), and the self-excitation of auroral arcs [*Ogino and Walker*, 1984; *Lyon et al.*, 1986; *Ogino*, 1986; *Fedder and*

Lyon, 1987; *Watanabe and Sato*, 1990; *Kageyama et al.*, 1992; *Usadi et al.*, 1993; *Fedder and Lyon*, 1995; *Fedder et al.*, 1995a; *Raeder et al.*, 1995; *Tanaka*, 1995; *Janhunen*, 1996; *Janhunen and Koskinen*, 1997; *Raeder et al.*, 1997; *Gombosi et al.*, 1998, 2000; *White et al.*, 1998; *Song et al.*, 1999]. A recent focus of MHD investigations is the study of magnetospheric "events." In these simulations the observed upstream solar wind conditions to are used to "drive" the magnetosphere-ionosphere system, and numerical predictions are compared with ground based or satellite observations [*Fedder et al.*, 1995b, 1998; *Raeder et al.*, 1998]. In addition to studies of the terrestrial magnetosphere, there have been several applications of MHD models to the study of coronal and solar wind plasma flows. This includes work by *Steinolfson* [1988, 1990, 1992, 1994], *Linker et al.* [1994], *Mikić and Linker* [1994], *Linker and Mikić* [1995], *Wang et al.* [1995], *Suess et al.* [1996], *Wu and Guo* [1997], *Wang et al.* [1998], *Guo and Wu* [1998], *Lionello et al.* [1998], *Dryer* [1998], *Odstrčil and Pizzo* [199a, 199b, 1999c], *Keppens and Goedbled* [1999], and *Suess et al.* [1999].

In this paper, the application of a new parallel adaptive mesh refinement (AMR) MHD model to the simulation of a complete fully three-dimensional space weather event is described. The simulation spans the initiation of the solar wind disturbance at the solar surface to its interaction with Earth's magnetosphere-ionosphere system. Numerical results are presented for a coronal mass ejection (CME) driven by local plasma density enhancement with an approximate "steady state" representation of the background solar wind. Coronal mass ejections, and the large magnetic clouds that are often associated with these solar wind disturbances, form a particularly important class of space weather event. These are massive highly transient events involving the expulsion of mass and magnetic field from the solar surface. Of the order of 10^{12} kg of plasma may be expelled from the solar surface during a typical CME event. More prevalent during solar maximum, CMEs originate in closed magnetic field regions of the corona and produce large-scale reconfiguration of the coronal magnetic field, which, in turn, generates large solar wind disturbances. Observations have established that CME disturbances are one major source of major geomagnetic storms at Earth. For example, during the solar maximum of 1978-1982 the majority of the most intense storms were associated with high-speed CMEs [*Tsurutani and Gonzalez*, 1997]. The simulation results described herein will illustrate the potential of the new MHD-based space weather model for enhancing the understanding of coronal physics, solar wind plasma processes, and space weather phenomena and lay the foundation for the future development of more comprehensive space weather prediction tools.

The organization of the paper is as follows. A brief out-

---

[1] Now at University of Toronto Institute for Aeropace Studies, Toronto, Ontario, Canada

line of the global 3-D MHD model is given in section 2. This outline includes details of the MHD equations that are solved and the parallel AMR scheme that is used to solve them. The details of the numerical method are given in Appendix A. Numerical results for the simulation of the CME space weather event are then described in sections 3 and 4. The steady state solution representing the initial state of the solar wind for conditions near solar minimum is presented in section 3 and the results for the density-driven CME are given in section 4. The CME results include discussions of the initiation process, CME propagation, structure of the magnetic cloud that forms, and CME plasma properties. In addition, the interaction of the CME with the coupled magnetosphere-ionosphere system is also discussed in section 4. A summary and some concluding remarks are given in section 5.

2. Global 3-D MHD Model

As discussed in section 1, a new global 3-D MHD model has been developed for the modeling of space weather events. An outline of the basic model is provided here, and further details are given in Appendix A.

In the global 3-D model, ideal MHD equations are used to describe the dynamic behavior of the coronal, solar wind, and magnetospheric plasma. These equations can be written in the following nondimensional nonconservative form:

$$\frac{\partial \tilde{\rho}}{\partial \tilde{t}} + \left(\tilde{\mathbf{u}} \cdot \tilde{\nabla}\right) \tilde{\rho} + \tilde{\rho} \left(\tilde{\nabla} \cdot \tilde{\mathbf{u}}\right) = 0 \,, \qquad (1)$$

$$\frac{\partial \tilde{\mathbf{u}}}{\partial \tilde{t}} + \left(\tilde{\mathbf{u}} \cdot \tilde{\nabla}\right) \tilde{\mathbf{u}} + \frac{1}{\tilde{\rho}} \tilde{\nabla} \tilde{p} = \frac{1}{\tilde{\rho}} \left(\tilde{\mathbf{j}} \times \tilde{\mathbf{B}}\right)$$
$$+ \tilde{\mathbf{g}} - \tilde{\mathbf{\Omega}} \times \left(\tilde{\mathbf{\Omega}} \times \tilde{\mathbf{r}}\right) - 2 \tilde{\mathbf{\Omega}} \times \tilde{\mathbf{u}} \,, \qquad (2)$$

$$\frac{\partial \tilde{p}}{\partial \tilde{t}} + \left(\tilde{\mathbf{u}} \cdot \tilde{\nabla}\right) \tilde{p} + \gamma \tilde{p} \left(\tilde{\nabla} \cdot \tilde{\mathbf{u}}\right) = (\gamma - 1) \tilde{Q} \,, \qquad (3)$$

$$\frac{\partial \tilde{\mathbf{B}}}{\partial \tilde{t}} - \tilde{\nabla} \times \tilde{\mathbf{u}} \times \tilde{\mathbf{B}} = 0 \,, \qquad (4)$$

where, for ideal MHD, the current density $\tilde{\mathbf{j}}$ is given by $\tilde{\mathbf{j}} = \tilde{\nabla} \times \tilde{\mathbf{B}}$. This equation set contains five equations describing the transport of plasma mass, momentum, and thermal energy as well as three equations describing the time evolution of the magnetic field given by Faraday's law. The nondimensional variables $\tilde{\rho}$, $\tilde{\mathbf{u}}$, $\tilde{p}$ and $\tilde{\mathbf{B}}$ correspond to the nondimensional plasma density, velocity, pressure, and magnetic field, respectively. They are related to their dimensional counterparts by $\tilde{\rho} = \rho/\rho_\circ$, $\tilde{\mathbf{u}} = \mathbf{u}/a_\circ$, $\tilde{p} = p/\rho_\circ a_\circ^2$,

and $\tilde{\mathbf{B}} = \mathbf{B}/\sqrt{\mu_\circ \rho_\circ a_\circ^2}$, where $\rho_\circ$ and $a_\circ$ are the density and ion-acoustic wave speed of a suitable reference solution state and γ is the specific heat ratio of the plasma. In (2), $\tilde{\mathbf{r}} = \mathbf{r}/\ell_\circ$, $\tilde{\mathbf{\Omega}} = \mathbf{\Omega}_\circ (\ell_\circ/a_\circ)$, $\mathbf{r}$ is the position vector, $\mathbf{\Omega}_\circ$ is the angular velocity of the Sun, $\ell_\circ$ is a reference length scale (in the present set of simulations, $\ell_\circ$ is the solar radius), and $\tilde{\mathbf{g}} = -\tilde{g} \left(\tilde{\mathbf{r}}/\tilde{r}^3\right)$, where $\tilde{g}$ is the nondimensional gravitational force at the solar surface. The volumetric heating term, $\tilde{Q}$, appearing on the right-hand side of (3) parametrizes the effects of coronal heating processes and heat and radiation transfer effects (see section 3).

We note that for the solar wind flow calculations, the MHD equations are solved in a rotating frame, which is convenient from a numerical perspective. Boundary conditions at the solar surface for "quasi-steady" (nonperturbed) solar wind are time-invariant, and a truly steady state solution for the solar wind can be obtained in the rotating frame. The additional source terms in the momentum equation represent the effects of centripetal and Coriolis acceleration forces and the solar gravitational force.

The preceding set of equations are solved using a newly developed parallel AMR scheme. Details of this algorithm are provided in Appendix A.

3. "Steady State" Model of Solar Wind

In this section a steady state model of the solar wind is developed that is representative of conditions near solar minimum. Considerable effort was devoted to constructing the steady state solution so as to provide a reasonable description of the time-averaged solar wind: (1) the computed three-dimensional solution for the magnetic field very near the Sun possesses high-latitude polar coronal holes, closed magnetic field flux tubes at low latitudes, and a helmet streamer structure with a neutral line and current sheet; (2) the Archimedean spiral topology of the interplanetary magnetic field is reproduced; (3) the observed two-stream nature of the solar wind is also reproduced with the numerical solution yielding fast and slow solar wind streams at high and low latitudes, respectively; and (4) the predicted latitudinal variation of solar wind plasma properties at 1 AU is in agreement with observational data. This solution provides the initial conditions for the coronal and solar wind plasma in the simulation of the CME space weather event described in section 4. While the magnetic field configuration is somewhat oversimplified, the initial solution represents a step toward developing more sophisticated models for the solar wind.

3.1. Physical Modeling

The corona is the outermost region of the solar atmosphere and is composed almost entirely of high-temperature ($T > 10^6$ K), low-density ($n_p \approx 10^{14}$ m^{-3}, where n_p is the proton number density), quasi-neutral proton-electron plasma. The expansion of the coronal plasma to large heliocentric distances is what forms the solar wind and carries the particles and fields out into interplanetary space at supersonic speeds. In order to model the transient behavior of the large-scale corona and solar wind and thereby gain an improved understanding of transient solar wind disturbances and their impact on space weather, a MHD solution representative of solar wind in the "steady state" is needed. The modeling of disturbances is then formulated as an initial value problem with initial conditions for the solar corona and solar wind plasma specified by the background steady state solution.

Observations have shown that the solar wind is in many respects a two state phenomenon [*Schwenn*, 1990; *Axford and McKenzie*, 1997; *McComas et al.*, 1998]. The so-called high-speed or fast solar wind is usually observed in the high latitude regions of the heliosphere, while the so-called slow solar wind is confined to relatively low latitudes. There is general agreement that the fast solar wind originates from polar coronal holes, and it is thought to be produced by additional but still poorly understood coronal heating processes occurring above the transition region but close to the Sun [*Axford and McKenzie*, 1996; *Fisk et al.*, 1999b]. Typical heights of the transition region above the base of the photosphere are between about 2500 and 3000 km. Near solar minimum the magnetic field at the solar surface has a dipolar nature, and the open field lines of the polar coronal holes originate from a region on the surface above ∼70° latitude. For the most part, closed field lines are confined to equatorial regions. At large heliocentric distances the topology of the magnetic field resembles an Archimedean spiral, as first predicted by *Parker* [1963]. The average single-fluid plasma properties of the fast solar wind at 1 AU include (1) a high flow velocity of about 750–880 km s^{-1} with small fluctuations about the average velocity; (2) a particle flux of about 2×10^8 cm^{-2} s^{-1}; (3) a radial component of the magnetic field of ∼2.8 nT; and (4) a plasma temperature, $T = T_e + T_p$, of about 3×10^5 K with $T_p/T_e \sim 2$. The fast wind achieves its asymptotic flow speed at around 10–15 R_s. The fast solar wind is dominant during periods of low solar activity, and it occupies the heliosphere above ∼30° heliolatitude.

The slow solar wind is confined to a narrow region near the heliospheric current sheet [*McComas et al.*, 1998; *Neugebauer et al.*, 1998]. This highly variable slow wind is thought to be formed from two plasma sources. First, material stored in closed magnetic field lines near the solar equator can be released into interplanetary space in an intermittent fashion through the opening of field lines by magnetic reconnection processes [*Fisk et al.*, 1999a; *Schwadron et al.*, 1999]. A second potential source of the slow solar wind is the overexpanded plasma from the edge of the polar coronal holes. There is considerable uncertainty in the relative contributions of these two sources to the slow solar wind. Observational data of Ulysses indicate that the transitions between the fast and slow solar winds were very sharp and are confined to a few degrees in heliolatitude [*McComas et al.*, 1998]. The average single-fluid properties of the slow solar wind at 1 AU are (1) a flow velocity of between 300 and 450 km s^{-1}; (2) a particle flux of about 3×10^8 cm^{-2} s^{-1}; and (3) a total plasma temperature of about 1.6×10^5 K.

With these features in mind, the "steady state" solar wind from 1 R_s to beyond 1 AU is simulated herein by assuming that, at 1 R_s (i.e., the top of the transition region or the base of the solar corona), the lower solar corona is a large, rigidly rotating reservoir of hot plasma with an embedded magnetic multipole field. The angular velocity of the reservoir is $\Omega_\circ = 2\pi/\mathcal{T}$, with a rotation period $\mathcal{T}$ of 26 days. The plasma temperature (the sum of the ion and electron temperatures) of the reservoir is taken to be $T_s = T_p + T_e = 2.85 \times 10^6$ K, and the plasma density is assumed to be $n_s = n_p = 1.5 \times 10^8$ cm^{-3}. The intrinsic solar magnetic field at the solar surface, $\tilde{\mathbf{B}}_\circ$, is defined in terms of a multipole expansion that includes terms up to the octupole moment. It is taken to have the form

$$
\begin{aligned}
\tilde{B}_{\circ_k} =\ & 3\frac{\tilde{M}_i \tilde{r}_i}{r^4}\frac{\tilde{r}_k}{\tilde{r}} - \frac{\tilde{M}_k}{\tilde{r}^3} \\
& + \frac{5}{2}\frac{\tilde{Q}_{ij}\tilde{r}_i\tilde{r}_j}{\tilde{r}^6}\frac{\tilde{r}_k}{\tilde{r}} - \frac{\tilde{Q}_{ik}\tilde{r}_i}{\tilde{r}^5} \\
& + 7\frac{\tilde{O}_{ijl}\tilde{r}_i\tilde{r}_j\tilde{r}_l}{\tilde{r}^8}\frac{\tilde{r}_k}{\tilde{r}} - 3\frac{\tilde{O}_{ijk}\tilde{r}_i\tilde{r}_j}{\tilde{r}^7}\,,
\end{aligned} \tag{5}
$$

where $\tilde{M}_i$ is the dimensionless dipole moment vector and $\tilde{Q}_{ij}$ and $\tilde{O}_{ijk}$ are the quadrupole and octupole moment tensors, respectively. In the present model of the steady state solar wind, $Q_{ij} = 0$, and the magnetic axis is tilted in the (x, z) plane such that

$$
\tilde{M}_x = -b_\circ \sin\theta_T \qquad \tilde{M}_y = 0 \qquad \tilde{M}_z = b_\circ \cos\theta_T\,. \tag{6}
$$

The tilt angle of the magnetic field is taken to be $\theta_T = -15°$, and $b_\circ$ and $\tilde{O}_{ijk}$ have values such that the solar magnetic field is azimuthally symmetric about the tilted magnetic axis and has a maximum field strength of 8.4 G at the magnetic poles and a strength of 2.2 G at the solar magnetic equator. The schematic diagram of Plate 1 illustrates the geometry of the solar magnetic field with respect to the rotation axis. The
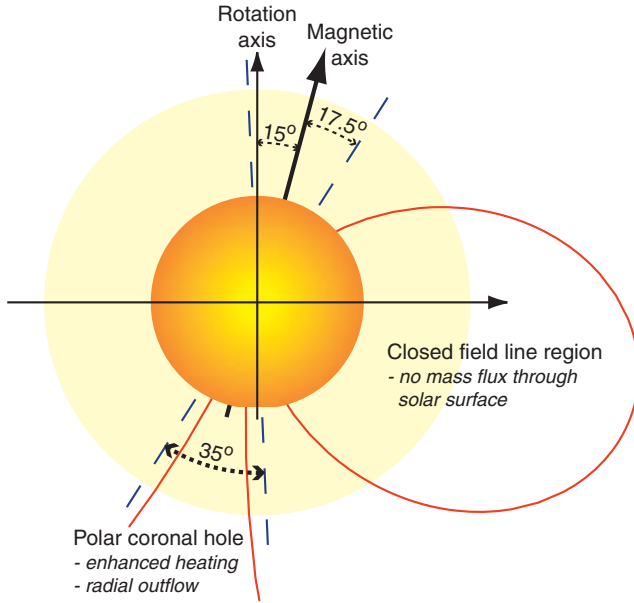
Plate 1. Schematic diagram depicting the geometric characteristics of the solar magnetic field and coronal hole models used in the steady state solar wind solution.

solar equatorial plane is taken to be perpendicular to the axis of rotation.

In the present model, volumetric energy input is needed in order to mimic the effects of heat conduction and energy dissipation above the transition region and reproduce a realistic solar wind. Thermal conduction, neglected in an ideal MHD description, is very important in the vicinity of the Sun and significantly impacts the acceleration of the solar wind [cf. *Steinolfson*, 1994; *Suess et al.*, 1996; *Hu et al.*, 1997; *Moore et al.*, 1999]. Moreover, coronal heating processes are not included self-consistently in the ideal MHD model. Although there is a general agreement about the need for additional coronal heating input [*Axford and McKenzie*, 1996; *Fisk et al.*, 1999b], the precise nature of the energy input is still debated [*Holzer et al.*, 1997]. Other effects such as radiation losses can also be important and affect the acceleration of the solar wind [*Rosner et al.*, 1978]. Some headway can be made without requiring the introduction of additional sources by adopting a value for the specific heat ratio near unity; however, a more realistic value for the specific heat ratio (i.e., $\gamma = 5/3$) is needed if the effects of adiabatic cooling at larger heliocentric distances are to be correctly modeled.

In order to overcome some of the limitations described above, enable a value of $\gamma = 5/3$ to be used in the calculations, and reproduce many of the observed plasma properties of the fast and slow solar wind streams, a volumetric heat-

ing function $\tilde{Q}$ has been introduced in (3). This function attempts to mimic the combined effects of energy absorption above the transition region, thermal conduction, and radiative losses. As the physical understanding of coronal heating processes remains limited, there is some freedom in choosing this source function. A function that includes both local energy deposition and losses is adopted herein. Furthermore, the heat source is taken to be latitude dependent, and it decreases exponentially with radial distance from the Sun. The latitudinal dependence of the heating function is chosen such that outflows are produced from polar coronal holes for $0° \leq \theta_m \leq 17.5°$, where θ_m is the heliocolatitude measured from the solar magnetic axis, no outflow and a closed field-line structure are produced for $17.5° \leq \theta_m \leq 90°$ (see Plate 1), and a realistic solar wind is obtained at large heliocentric distances, having both fast and slow streams. Specifically, the volumetric heating function $\tilde{Q}$ is assumed to have the form

$$\tilde{Q} = \tilde{\rho}\tilde{q}_\circ \exp\left[-\frac{\left(\tilde{r} - \tilde{R}_\circ\right)^2}{\sigma_\circ^2}\right]\left(\tilde{T}_\circ - \gamma\frac{\tilde{p}}{\tilde{\rho}}\right), \quad (7)$$

where $\tilde{T}_\circ = 1.75$ poleward from a critical colatitude $\theta_\circ(\tilde{r})$ and $\tilde{T}_\circ = 1$ equatorward of $\theta_\circ(\tilde{r})$. In addition, $\tilde{q}_\circ = 25$, $\tilde{R}_\circ = 1$, and $\tilde{r}$ is the heliocentric radius. It can be seen that the heating is proportional to $(T_\circ - T)$, where $T_\circ$ is a prespecified "target" temperature. The target temperature is taken to be $T_\circ = 1.75T_S$ inside the coronal hole and $T_\circ = T_S$ outside. As indicated in Plate 1, the coronal hole boundary is taken to be located at $\theta_m = 17.5°$, and the functions $\theta_\circ(\tilde{r})$ and $\sigma_\circ(\tilde{r}, \theta_m)$ are defined so as to produce the desired spatial distribution of coronal heating. They have the following limits:

$$\theta_\circ(\tilde{r} = 1) = 17.5° \qquad \theta_\circ(\tilde{r} \to \infty) = 90°, \quad (8)$$

$$\sigma_\circ(\tilde{r}, \theta_m = 0) = 9 \qquad \sigma_\circ(\tilde{r}, \theta_m > \theta_\circ) = 4.5. \quad (9)$$

This leads to a scale height for the volumetric heating that slowly varies from $\sim 4.5\ R_S$ near the equator to about $\sim 9\ R_S$ at the poles. Note that the heating function has a sharp gradient at the edge of the coronal hole; however, the finite resolution of the computational grid ($\sim 5°$ near the Sun in the present calculations) limits the sharpness of this transition. The volumetric heating function of (7)–(9) is clearly empirical in nature and involves several parameters. The overriding criteria for specifying the values of these parameters has been the desire to reproduce many of the observed global plasma properties of the fast and slow solar wind streams at 1 AU.

3.2. Computational Mesh

Using the parallel AMR scheme of Appendix A, a solution for the steady state background solar wind was obtained. For this calculation the computational domain was a heliocentric rectangular box defined in the rotating frame by -32 $R_s \leq x \leq 224\ R_s$, $-192\ R_s \leq y \leq 192\ R_s$, $-192\ R_s \leq z \leq 192\ R_s$ with the z axis aligned with the solar rotational axis and the x and y axes lying in the plane of the solar equator. The adapted computational grid consisted of 15,768 self-similar $4{\times}4{\times}4$ blocks and 1,009,152 cells with eight refinement levels and a minimum cell size at the solar surface of 1/16 R_s. For the time-dependent calculation of the space weather event to be described later, this same grid was used to initiate the calculations. The grid was then dynamically adapted to the varying local MHD solution according to the refinement criteria of (A10) such that the number of cells in the computational mesh varied from just under 800,000 to well in excess of 2,000,000.

3.3. Boundary Conditions

In order to obtain the steady state solar wind solution, boundary conditions are required at the inner boundary of the solution domain, defined by the solar surface at $r = 1$ R_s, and outer boundaries, defined by the outer edges of the rectangular solution domain. The procedure for prescribing boundary conditions at the solar surface was made dependent on local flow conditions. Plasma was permitted to freely leave the reservoir, but no "backflow" was allowed. In addition, the magnetic field was specified by the multipole expansion for the intrinsic magnetic field at the interface given by (5). In the rotating frame the following procedure was adopted: for $\tilde{u}_r > 0$,

$$\tilde{\rho} = 1 \qquad \tilde{p} = \frac{1}{\gamma} \qquad \tilde{\nabla} \cdot (\tilde{\rho}\tilde{\mathbf{u}}) = 0 \qquad \tilde{\mathbf{B}} = \tilde{\mathbf{B}}_\circ, \quad (10)$$

and for $\tilde{u}_r < 0$,

$$\frac{\partial \tilde{\rho}}{\partial r} = 0 \qquad \frac{\partial \tilde{p}}{\partial r} = 0 \qquad \tilde{\mathbf{u}} = 0 \qquad \tilde{\mathbf{B}} = \tilde{\mathbf{B}}_\circ, \quad (11)$$

depending on whether the flow was toward or away from the solar surface.

At the outer boundaries of the rectangular solution domain, the solar wind flow is essentially super-fast (and hence super-Alfvénic). Simple zero-gradient (Neumann-type) or constant extrapolation boundary conditions are therefore appropriate and are used to specify the plasma properties at the outer boundary.

It should be noted that the use of a Riemann solver in the evaluation of the numerical flux function of the parallel AMR scheme (refer to Appendix A) greatly simplifies the implementation of numerical boundary schemes, for it is always well posed. By using the Riemann solver, the boundary schemes are generally well posed and consistent with the propagation of solution characteristics. Physical correctness and accuracy of the boundary schemes remain the only concerns.

3.4. Time-Invariant Solar Wind Solution

The steady state solar wind was obtained by using the parallel AMR scheme. Local time stepping was used to speed up convergence of the numerical solution to the desired steady state and steady state result was obtained after $\sim$180,000 iterations (local time steps). Plate 2 depicts a three-dimensional representation of the predicted pre-event steady state solar wind solution in the vicinity of the Sun. The color shading represents computed values of the logarithm of the magnitude of the magnetic field, $\log(\tilde{B})$, for the solution in the meridional and equatorial planes. The solid lines are magnetic field lines: magenta denotes the last closed field lines, red is open field lines expanding to the interplanetary medium just above the heliospheric current sheet, and, finally, white lines show open magnetic field lines in the (y, z) plane. The narrow dark blue region shown in Plate 2, which also coincides with regions of higher mesh refinement, corresponds to the beginning of the heliospheric current sheet. The current sheet originates in the region where the equatorial portion of the closed magnetic field lines become highly stretched and then extends outward throughout the rest of the solution domain. Because of the combined effects of magnetic tilt and solar rotation, the current sheet is tilted with respect to the rotation axis, is deformed, and resembles a "ballerina skirt."

Inspection of Plate 2 reveals that the solution within $r = 10\ R_s$, which is dictated by a balance of pressure, magnetic, gravitational, and inertial forces, has some similarities to the now classical solution obtained by *Pneuman and Kopp* [1971]. There are regions of open and closed magnetic field lines, and this leads to the formation of a "helmet" streamer configuration, with a neutral line and current sheet. (Note that whether a field line is open or closed is not directly specified in the numerical solution. Depending on the strength of the magnetic field at the solar surface, the specified plasma properties at 1 R_s, and additional volumetric heating, field lines are either open or closed. Open field lines are produced in the solution by the outflowing plasma that drags the field lines out into interplanetary space.) However, unlike the Pneuman-Kopp model, the present solution more correctly mimics the two-state nature of the solar wind. Fast solar wind ($\sim$800 km s^{-1}) originating from polar coronal holes is produced above $30°$ in heliolatitude, slow solar wind ($\sim$400 km s^{-1}) is produced near the solar equator at
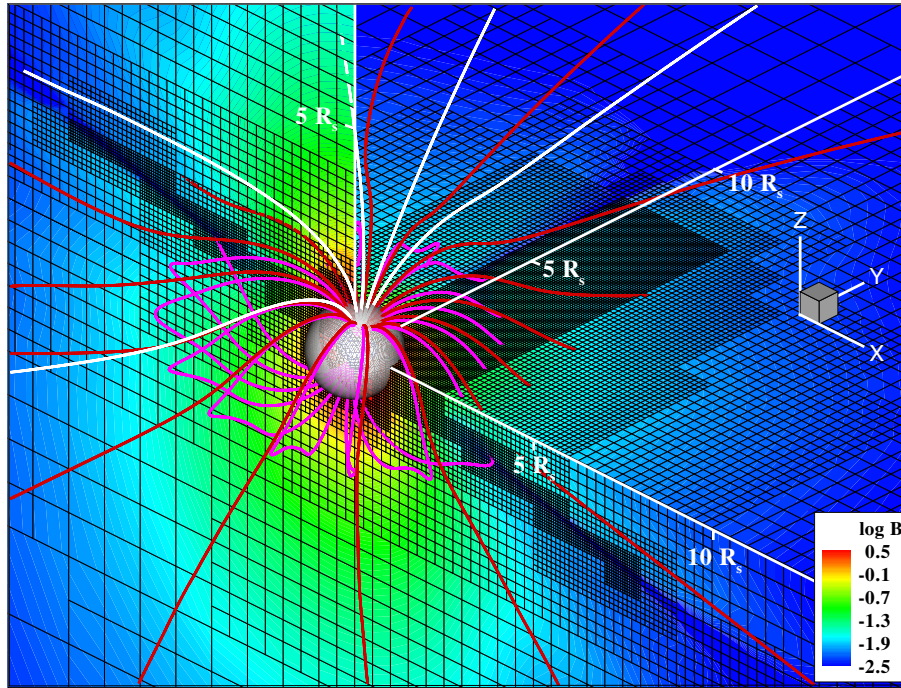
Plate 2. Three-dimensional representation of the steady state solar wind solution. The color shading represents $\log(B)$ in the (x, z) and (x, y) planes. The black lines are the computational mesh, and the colored solid lines are magnetic field lines: magenta denotes the last closed field lines, red is open field lines expanding to the interplanetary medium just above the heliospheric current sheet, and, finally, white lines show open magnetic field lines in the (y, z) plane.

lower latitudes, and reasonable values for the plasma properties and interplanetary magnetic field are obtained at 1 AU.

Adopting an expanded field of view, Plate 3 shows the larger-scale structure of the predicted interplanetary magnetic field. Again, the color shading represents computed values of the logarithm of the magnitude of the magnetic field. The top panel shows a three-dimensional rendering of the magnetic field lines in which the three different sets of colored lines (magenta, white, and red) represent field lines leaving the field of view at three different heights above the solar equatorial plane. The bottom panel of Plate 3 shows the projection of the red field lines from the top panel onto the plane of heliographic equator. It is evident from Plate 3 that the simulated steady state solution for the solar wind yields an interplanetary magnetic field with an Archimedean or Parker-like spiral structure. In particular, the magnetic field line projections of the bottom panel clearly depict the spiral shape of the large-scale magnetic field. Nevertheless, from the top panel it can be seen that, unlike Parker's solution, the tilt of the solar magnetic axis results in spiral field lines that connect to regions of very different heliolatitides.

The two-state nature of the computed solution is clearly depicted in Plate 4. Shown is a polar diagram of the computed solar wind speed at 1 AU as a function of heliolatitude. Flow speed profiles are given for the $x = 0$ (green lines) and $y = 0$ (black lines) meridional planes. In both cases, there is a transition from one solar wind regime to another at midlatitudes. The width of the transition is to some extent controlled by the thickness of the heliospheric current sheet. The simulation results are quite consistent with Ulysses observations [*McComas et al.*, 1998], as can be seen by comparison to the Ulysses Solar Wind Observations Over the Poles of the Sun (SWOOPS) proton velocity data also shown in Plate 4. (The Ulysses/SWOOPS data were obtained from the European Space Agency (ESA) Archive at http://helio.estec.esa.nl/ulysses/archive/). It is interesting that because of the tilt of the magnetic axis, the simulated meridional speed profiles are different in the two meridional planes. Although at high latitudes (in the fast solar wind region) the two meridional profiles have practically identical speeds, at lower latitudes the meridional profiles differ by as much as 200 km s^{-1}. When combined with solar rotation, this difference might lead to rapid transitions from a "slow" to "fast" solar wind at midlatitudes.
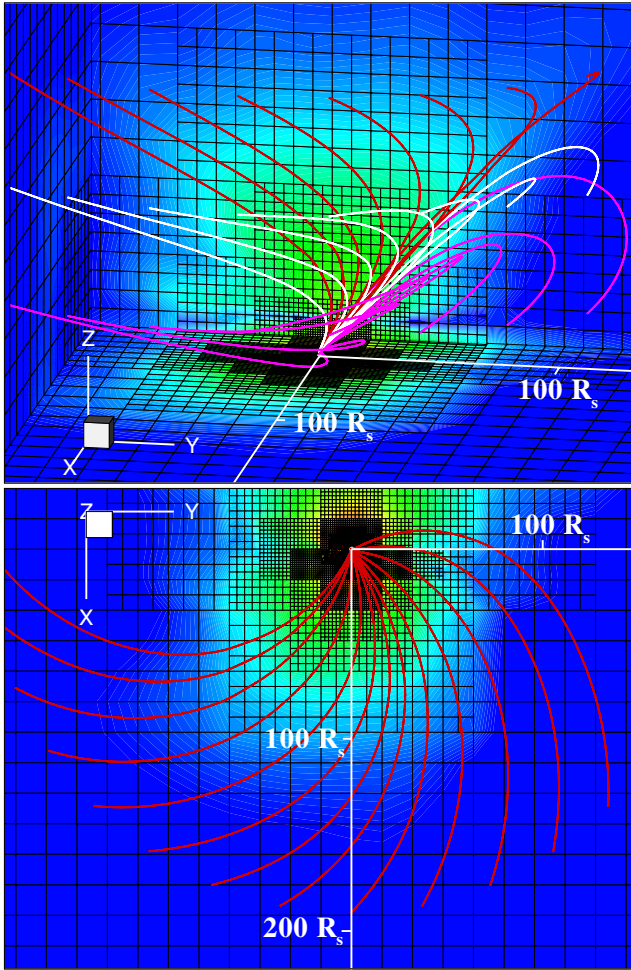
Plate 3. Structure of the interplanetary magnetic field for the steady state solar wind solution.

Plate 4. Polar plot of computed solar wind speed at 1 AU compared to Ulysses Solar Wind Observations Over the Poles of the Sun (SWOOPS) observations of proton velocity [*McComas et al.*, 1998]. The black and green lines represent simulation results in the $x = 0$ and $y = 0$ meridional planes, respectively.

Plate 5. Latitudinal variation of computed solar wind number density at 1 AU compared to Ulysses/SWOOPS observations of proton number density [*McComas et al.*, 1998]. The black and green lines represent simulation results in the $x = 0$ and $y = 0$ meridional planes, respectively.

Further comparisons between the solar wind plasma properties predicted by the MHD simulation and the observational data of the Ulysses/SWOOPS instrument [*McComas et al.*, 1998] are given in Plates 5 and 6. The latitudinal variation of the proton number density and temperature at 1 AU are shown in the two graphs. The black and green curves again represent the simulation results in the $x = 0$ and $y = 0$ meridional planes, respectively. The Ulysses/SWOOPS observations are represented by the thick blue and red lines. For the MHD calculations the proton temperature is obtained from the plasma temperature by simply assuming that $T_p = T/2$. The Ulysses/SWOOPS data, collected at various heliocentric distances, have been normalized to 1 AU. The comparisons shown in the two plates reveal a good overall agreement between the observations and simulation results. In particular, the simulated temperature profile approximates
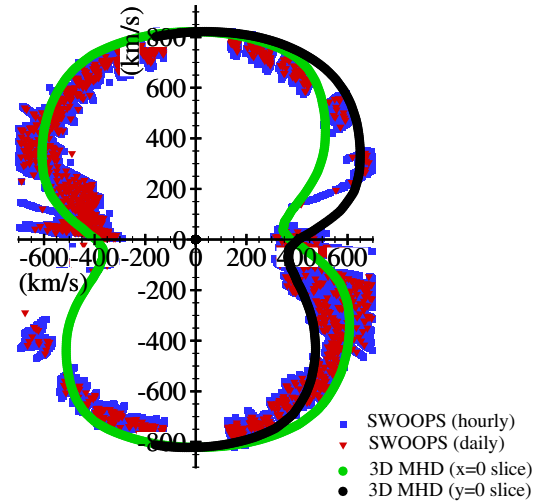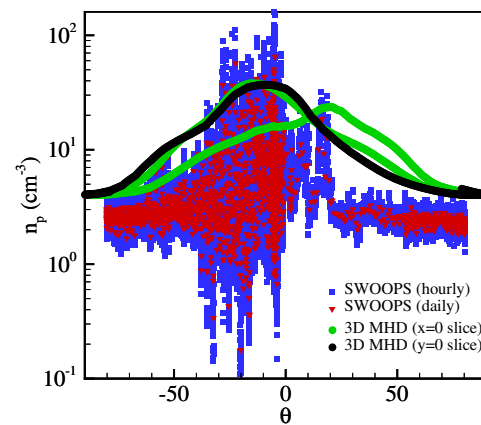
the observations quite well. The calculated density seems to be somewhat higher than the Ulysses/SWOOPS obser-
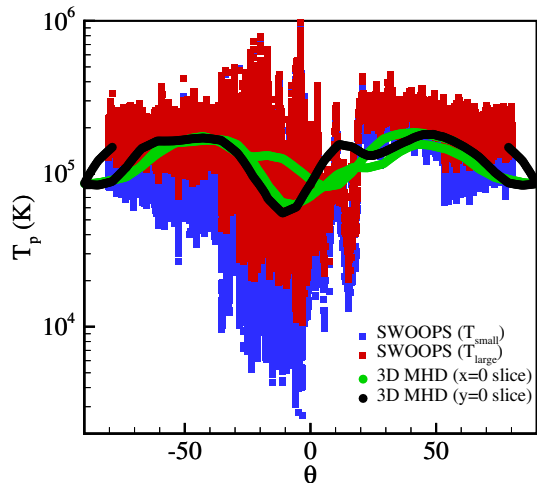
Plate 6. Latitudinal variation of computed solar wind proton temperature ($T_p = T/2$) at 1 AU compared to Ulysses/SWOOPS observations of proton temperature [*Mc-Comas et al.*, 1998]. The black and green lines represent simulation results in the $x = 0$ and $y = 0$ meridional planes, respectively.

vations, but not unreasonably so. The agreement between the simulation results and observations could be further improved by performing some additional "fine tuning" of the volumetric heating function and the specified plasma parameters at 1 R_s, but this was deemed to be unnecessary for the present study.

It was stated earlier that the slow solar wind is thought to be an inherently transient phenomenon arising from two sources: (1) the overexpanded plasma associated with streamers near the edges of coronal holes and (2) plasma associated with closed magnetic field lines that become open through reconnection [*Fisk*, 1996; *Schwadron et al.*, 1999]. In the present MHD model the primary source of the slow solar wind is the overexpanded plasma flow associated with the streamers. This is because there is almost no mass flux emerging from the closed field line regions on the solar surface and most of the slow solar wind plasma flows out from the solar surface along open field lines that originate close to the open–closed field line boundary. However, it should be noted that, for numerical stability, the procedure used in the discretization of the MHD equations introduces numerical dissipation. Although our solution method is designed to minimize the dissipation that is introduced, the finite numerical resistivity results in the reconnection of the last closed magnetic field lines at the top of the helmet-like structure.

This reconnection process continues along the heliospheric current sheet. The reconnection process at the top of the helmet streamers acts as a secondary source of slow solar wind near the magnetic equator, and, in this respect, numerical resistivity is helpful in "mimicking" some of the real physical processes taking place in the corona.

A summary of the fast and slow solar wind plasma properties at the solar surface and at 1 AU is given in Table 1. In Table 1 $\beta = 2\tilde{p}/\tilde{B}^2$ is the plasma beta. Overall, the steady state global MHD solution of the solar wind developed in this section provides a very reasonable description of the inner heliosphere for conditions near solar minimum. By using physically reasonable input parameters near the Sun and incorporating a physically motivated volumetric heating function, a solution out to 1 AU has been obtained that is in good overall agreement with the average observed solar wind features.

4. Simulation of a Space Weather Event

In this section the results of the numerical simulation of a CME driven space weather event are given. This includes a description of the CME initiation process and a presentation of the important features of the simulated event. The propagation of the CME through interplanetary space leading to the formation of a magnetic cloud and the CME interaction with the terrestrial magnetosphere are also discussed. The long-term overarching objective of this research is to develop global space plasma models that can accurately track the initiation of CMEs (and/or other space weather events) at the solar surface, follow their propagation through interplanetary space, and subsequently predict their impact on the magnetosphere. The results and modeling described herein represent but a starting point for this endeavor.

4.1. Density-Driven CME Initiation Model

It was stated in section 1 that CMEs produce large-scale reconfiguration of the coronal magnetic field and generate large solar wind disturbances that appear to be the primary cause of the major geomagnetic storms at Earth. Nevertheless, the physical mechanisms involved in the initiation of CMEs are not well understood. Many scenarios have been put forth for their release. Early on it was suggested that thermally driven pressure pulses from solar flares drive the release [*Dryer et al.*, 1979], yet more recently it is felt that it is the large-scale destabilization of the coronal magnetic field that initiates CMEs. *Low* [1990] and *Hundhausen* [1999] have considered the release of CMEs as a two-step process: first, there is a CME that opens up an initially closed coronal magnetic field; this is followed by a flare resulting from the reconnective closing of field lines trailing

Table 1. Simulated Steady State Solar Wind Plasma Properties

Quantity	Units	$1\ R_s, \theta = -15°$	$1\ R_s, \theta = 75°$	$1\ \text{AU}, \theta = -15°$	$1\ \text{AU}, \theta = 75°$
n_p	m^{-3}	0.82×10^{14}	10^{14}	38×10^6	4.1×10^6
u_p	km s^{-1}	0	25	370	830
$n_p u_p$	$\text{m}^{-2}\ \text{s}^{-1}$	0	2.5×10^{18}	14×10^{12}	3.4×10^{12}
B		2.2 G	8.4 G	—	2 nT
β		0.1	0.007	—	2
V_A	km s^{-1}	495	1885	—	22

the ejecta [*Hirayama*, 1974; *Kopp and Pneuman*, 1976; *Low*, 1994]. Another scenario put forth for the formation and release of CMEs involves the buildup of magnetic energy and subsequent destabilization of the field due to the quasi-static shearing of the footprints of closed magnetic field lines on the solar surface [*Low*, 1977; *Wu et al.*, 1983; *Mikić et al.*, 1988; *Mikić and Linker*, 1994]. This effect is likely to be a trigger mechanism but is not, by itself, sufficient to explain the CME phenomenon [*Linker and Mikić*, 1995; *Low*, 1996]. Finally, it has been suggested that the onset of CMEs may be produced by the emergence of magnetic flux ropes that gain energy as they are continually stressed and deformed by chromospheric and photospheric motions [*van Ballegooijen and Martens*, 1990]. Prior to eruption, the flux ropes are confined by the large mass in the flux tubes, but when confinement fails CMEs are initiated owing to the magnetic buoyancy of the ropes [*Low*, 1981; *Fisher and Poland*, 1981; *Low et al.*, 1982; *Illing and Hundhausen*, 1986]. Recently, numerical methods and global MHD models have begun to play an important role in efforts to understand CME initiation processes, and numerical studies of both magnetic shear and helical flux rope emergence initiation processes have been carried out (see for example, the work by *Mikić and Linker* [1994], *Linker and Mikić* [1995], *Wu and Guo* [1997], and *Guo and Wu* [1998]).

After release, CMEs accelerate and become part of the outward flow of the solar wind. They either are accelerated by the solar wind so as to come into equilibrium with the ambient wind or act as drivers moving faster than the background solar wind. Close to the Sun, the typical dimension of a CME is less than a solar radius. As the CMEs propagate outward from the corona, they expand dramatically and may extend over tenths of an AU by the time Earth's orbit is reached. The topology of the magnetic field within the CME evolves as it propagates outward into unique structures that reflect the original field configuration from which the CME was generated (i.e., it is expected that magnetic helicity is preserved [*Chen et al.*, 1997]). Moreover, many, if not all, CMEs are associated with magnetic clouds, and the plasma properties within these clouds, can differ substantially from those of the ambient solar wind. Several recent numerical studies of coronal flows and CME evolution through interplanetary space have been performed, as described in the work by *Steinolfson* [1992, 1994], *Linker et al.* [1994], *Mikić and Linker* [1994], *Linker and Mikić* [1995], *Suess et al.* [1996], *Wang et al.* [1998], *Wu and Guo* [1997], *Guo and Wu* [1998], *Lionello et al.* [1998], *Dryer* [1998], and *Odstrčil and Pizzo* [1999a, 1999b, 1999c].

In the present study, a simplified model for the initiation of the CME is adopted. Using the solution of the nominal background solar wind described above as the initial state of the solar wind, a CME was initiated by introducing a localized isothermal density (and consequently pressure) enhancement at the solar surface. Although somewhat oversimplified, this model simulates what is thought to be a key feature of CME initiation processes, that is, the mass loading of the solar atmosphere. In the emerging flux rope model an important aspect of the CME initiation process is the loading of the solar atmosphere with additional plasma brought up from the lower corona and supported by the emerging magnetic field. The subsequent slow draining of plasma from the flux ropes is what destabilizes the magnetic field (owing to magnetic buoyancy effects) and causes CME onset. As will be shown, the density-driven model used herein simulates the mass-loading process and leads to an enhanced plasma density within the flux tubes of the closed field lines of the solar magnetic field, prior to the release of the CME.

The isothermal density enhancement on the solar surface was prescribed by locally increasing the values of the density and pressure by a factor f_{CME}:

$$f_{\text{CME}} = \begin{cases} 1 + f_r \exp\left[-\dfrac{(t-t_1)^2}{\sigma_t^2}\right] & t < t_1\,, \\ 1 + f_r & t_1 \leq t \leq t_2\,, \\ 1 + f_r \exp\left[-\dfrac{(t-t_2)^2}{\sigma_t^2}\right] & t > t_2\,, \end{cases} \quad (12)$$

where

$$f_r = 134 \exp\left[-\frac{(\mathbf{r} - \mathbf{r}_{\mathrm{CME}})^2}{\sigma_r^2}\right] \qquad (13)$$

and where we used $t_1 = 2$ hours, $t_2 = 10$ hours, $\sigma_t = 1$ hour, $\mathbf{r}_{\mathrm{CME}} = [0.9798\,R_S, 0, 0.20\,R_S]^\mathsf{T}$ and $\sigma_r = 0.13\,R_S$. This function of location and time produced local increases in the density and pressure by a factor of up to maximum of 135 in a small region on the solar surface $\sim$0.10 R_S wide just above the equator at a latitude of $11.5°$ (colatitude of $78.5°$). The density and pressure were gradually increased over a 2-hour period to maximum of a 135:1 increase, this increase was maintained for eight hours, and then the density and pressure were returned to their original values over a period of 2 hours.

4.2. Embedded Magnetosphere-Ionosphere Model

The terrestrial magnetosphere is a complex nonlinear system. The solar wind plasma properties and direction of the interplanetary magnetic field (IMF) exercise fundamental control over the large-scale configuration of the magnetosphere. The magnetospheric topology, in turn, controls the entry of mass, momentum, energy, and magnetic flux into the magnetosphere. The dynamic solar wind also controls the level of geomagnetic activity in the near Earth space environment and produces various transition layers, the extended geomagnetic tail and plasma sheet, current systems, and auroral phenomena. In order to predict in a self-consistent manner the dynamic response of the Earth's magnetosphere to the changing solar wind conditions associated with the simulated density-driven CME event, a complete MHD model of the magnetosphere-ionosphere system has been embedded within the CME space weather event model. As in the heliosphere model, the magnetosphere-ionosphere model employs the parallel AMR scheme of Appendix A to solve the 3-D MHD equations and thereby predict the configuration of the magnetosphere and properties of the magnetospheric plasma. Basic properties of the present magnetosphere model have been described by *Gombosi et al.* [1998, 2000] and *Song et al.* [1999].

The main features of the embedded magnetosphere-ionosphere model are as follows:

1. Earth's intrinsic magnetic field is represented by a non-tilted, nonrotating magnetic dipole field with an equatorial surface field of 0.3 G and magnetic axis perpendicular to the Sun-Earth direction.

2. Earth is assumed to be moving in a perfectly circular orbit about the Sun with an orbital radius of $215.5\,R_S$ and an orbital period of 365.25 days. The orbital plane is inclined at an angle of $7.25°$ to the solar equator with a node line aligned with the x axis and the maximum and minimum ex-

cursions of the planet in z direction occurring in the $y = 0$ plane. Earth's initial position at $t = 0$ in the numerical simulation is taken to be $\mathbf{r}_e = [209.23\,R_S, 43.94\,R_S, 27.18\,R_S]^\mathsf{T}$ which corresponds to a heliospheric latitude of $7.24°$ (colatitude of $82.76°$). This initial position was selected to ensure that the Earth was in the path of the simulated CME.

3. Magnetosphere-ionosphere coupling is accounted for by using a height-integrated electrostatic ionosphere model, which provides closure of the magnetospheric current system at the ionospheric boundary. In particular, Ohm's law is applied to a thin spherical shell [*Goodman*, 1995; *Amm*, 1996]. An elliptic equation for the ionospheric electric potential is solved on this shell involving height-integrated conductivities (conductances). The resulting ionospheric potential solution provides boundary conditions for the plasma convection velocity in the MHD solution at the magnetosphere-ionosphere interface. The magnetospheric current and ionospheric electric field are mapped along dipole field lines between the inner boundary of the magnetosphere and the ionospheric surface, thereby providing coupling between the magnetosphere and ionosphere.

4. Inner boundary conditions for the magnetosphere are imposed at 3 R_e and the height-integrated ionosphere model is solved at 1.017 R_e. A simplified model for the ionospheric conductances was used. The Petersen, Hall, and field-aligned conductances were taken to be constant with values of 5, 0, and 5,000 S, respectively.

5. A solution for the magnetosphere was obtained on a rectangular computational domain that is moving with the orbiting Earth and defined by $-384\,R_e \leq x \leq 128\,R_e$, $-128\,R_e \leq y \leq 128\,R_e$, $-128\,R_e \leq z \leq 128\,R_e$. The computational mesh contained eight levels of refinement and was composed of 2,004 self-similar blocks of $4 \times 4 \times 4$ cells for a total of 128,256 computational cells.

Coupling of the heliosphere and magnetosphere is required in order to achieve a self-consistent solution. In the present calculations the heliosphere simulation, including the modeling of the solar wind and CME, was coupled to the embedded magnetosphere using a one-way coupling procedure. In particular, changes in the solar wind plasma properties and IMF upstream boundary of the embedded magnetosphere were calculated at each time step by using the interpolated solution from the heliosphere simulation (these changes were due to both the rotation of the tilted solar magnetic field and the passage of the density-driven CME). The magnetosphere solution was not fed back into the heliosphere calculation. By using the fully three-dimensional heliospheric model to drive the embedded magnetospheric model, a self-consistent solution of the space weather event was achieved. The physical justifications for the use of one-way coupling are twofold: (1) the scale of the mag-

netosphere solution domain is very small compared to the scale of the heliospheric solution domain, and (2) the solar wind flow is superfast (and hence both supersonic and super-Alfvénic) at Earth. For these reasons, the solar wind interaction with Earth does not impact the upstream heliospheric solution and has negligible impact on the global solar wind solution.

4.3. Density-Driven CME Solution

Numerical results for the CME driven by the local plasma density enhancement now follow. The length of the entire CME computation was 120 hours of simulated time starting with the pre-event steady state solar wind solution and initiation of the CME at $t = 0$. The average size of the time steps used in the heliospheric calculation was $\sim$3 s, and 150,000 time steps were required to reach $t = 120$ hours. The calculation required slightly more than 20,000 processor hours and ran about $\sim$3 faster than real time on a 512-processor Cray T3E-600 located at NASA Goddard Space Flight Center.

The embedded magnetosphere model was "turned on" at $t = 70$ hours, just after the leading edge of the interplanetary transient reached Earth orbit, and was continued for a total of 27 hours until $t = 97$ hours. As the ratio of the solar and terrestrial radii is large ($R_s/R_e \approx 110$) and the strength of the terrestrial magnetic field is large compared to the prevailing IMF, the time step for the magnetospheric calculation was much smaller than that used in the heliospheric calculation ($\approx$0.13 s), and the magnetospheric calculation required $\sim$760,000 time steps and 14,000 processor hours on a Cray T3E-600 computer. Using 512 nodes, the total "wall-clock" time for the simulation was about equal to the total simulated time of 27 hours. The resolution of the heliospheric computational grid at Earth was between 10 and 40 R_s; therefore the time resolution of any solar wind feature at Earth in the heliospheric simulation was a few hours.

A three-dimensional representation of the computed magnetic field configuration 9 hours after the initiation of the CME is shown in Plate 7. The color shading represents computed values of the logarithm of the magnitude of the magnetic field, $\log(B)$, for the solution in the meridional and equatorial planes. The solid white lines are open magnetic field lines, and the magenta lines represent closed field lines with both ends connected to the Sun. The solution shown in Plate 7 can be compared to the pre-event state of the solar corona depicted in Plate 2. At $t = 9$ hours the density enhancement at the solar surface used to initiate the CME is already in the declining phase; nevertheless, the density maximum at the solar surface is still more than 100 times higher than the original background density.

Plates 8 and 9 show snapshots of the numerical solution of the CME in the near solar region ($r < 32\ R_s$) at $t = 1$, 4.5, 9, and 13.5 hours. Plates 10 and 11 show a similar set of solution snapshots on a larger scale ($r < 124\ R_s$) at $t = 6$, 12, 24, and 36 hours. The color shading used in Plates 8–11 represents the plasma mass flux normalized to 1 AU, while the white solid lines are magnetic "streamlines" drawn in two planes: the $y = 0$ meridian and the $z = 0$ equatorial plane. The magnetic streamlines are generated by using the two-components of the magnetic field in the plane of interest, and the third component of the magnetic field (perpendicular to the plane) is neglected. The streamline topology does therefore not fully characterize the magnetic field line topology, and one must be careful with interpretations. In general, the magnetic field will possess a nonzero component normal to the plane, and the fully three-dimensional field lines will therefore pass through (into and out of) the viewing plane. The primary advantage of using magnetic streamlines is that they are relatively easy to visualize. Cross-sectional patterns like those in Plates 8–11 are typically characterized by critical points, i.e., points at which the component of the magnetic field in the plane is zero. These critical points may be classified as stable or unstable nodes, saddles, centers, or stable or unstable spirals. While it is easy to misinterpret such critical points, as the normal component has been ignored, they do correspond to certain physical situations of interest. For example, a node in Plates 8–11 corresponds to the turning of the the magnetic fields lines from a three-dimensional orientation to one that is perpendicular to the viewing plane.

Plates 8–11 reveal much about the time history of the formation of the CME and its evolution as it propagates through the inner heliosphere. It can be seen that the density enhancement first leads to the "filling" of the closed magnetic flux tubes with additional plasma and subsequent expansion of the closed field line region. The plasma β in the enhancement region becomes quite large, and the closed field lines became stretched as they are "carried" outward by the plasma. After a period of time the closed field lines are unable to contain the additional plasma, and the density disturbance disrupts the closed magnetic configuration. The resulting CME then moves more rapidly through the inner corona and propagates outward into interplanetary space, dragging out closed field lines with it and disrupting the heliospheric current sheet as it moves. The disruption of the Parker spiral is also clearly evident in Plate 11. As the CME in this simulation is purely driven by a density enhancement, the emerging magnetic field is largely poloidal (having only radial and latitudinal components) without any significant helicity (twist). This is a clear limitation of the present calculation, as the helicity of the emerging magnetic flux is thought to be an important aspect of CMEs. The mag-
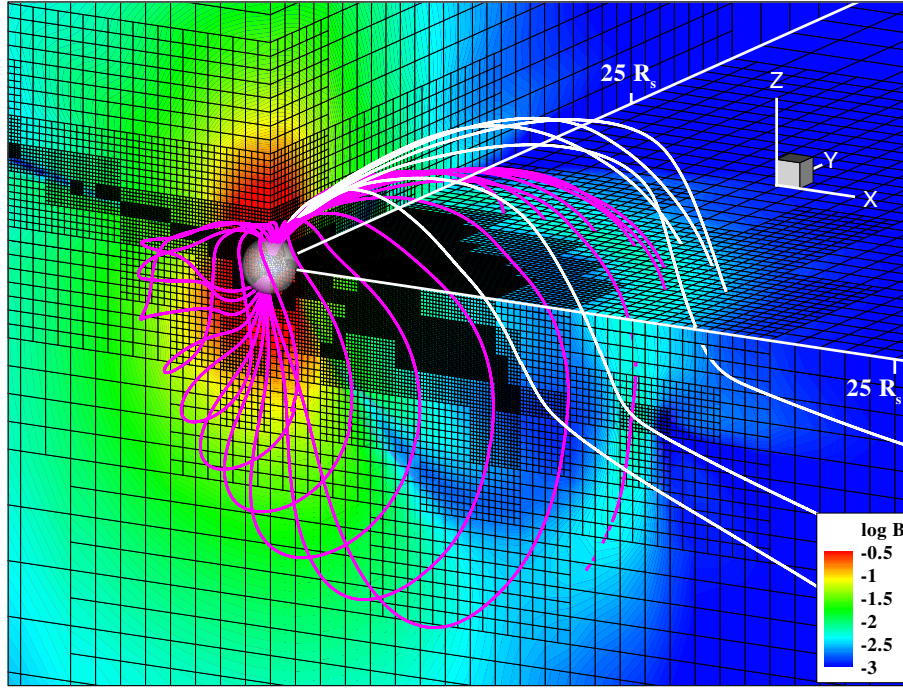
Plate 7. Three-dimensional configuration of magnetic field lines 9 hours after the initiation of the CME. The color shading represents $\log(B)$ in the (x, z) and (x, y) planes. The black lines are the computational mesh, white lines are open magnetic field lines, and magenta lines represent magnetic field lines with both ends connected to the Sun.

netic helicity H of a magnetic field configuration is defined in terms of the volume integral $H = \int \mathbf{A} \cdot \mathbf{B} dV$, where $\mathbf{A}$ is the magnetic vector potential and $\mathbf{B} = \nabla \times \mathbf{A}$. The helicity is a measure of the structural complexity of the magnetic field, and it is expected that the magnetic helicity is conserved in flux ropes that emerge and leave the Sun. The boundary conditions used to produce the density enhancement and trigger the CME at the solar surface do not impose any helicity in the magnetic field emerging from the solar surface, and so the helicity of the CME magnetic field is negligible.

A magnetic cavity propagates behind the front of the simulated disturbance, which moves at velocities nearing 560 km s^{-1}. The magnetic cavity is indicated by the decrease in the magnetic field strength behind the leading edge of the outward moving disturbance in Plate 7. A plot of the position of the leading edge of the CME in the plane of the current sheet as a function of time is given in Figure 1 and it clearly illustrates the two-step release process and two nearly constant speeds at which the CME moves during the first 24 hours following onset.

Somewhere between 17 and 19 hours into the simulation, the density and pressure enhancements at the solar surface have completely diminished and the CME field lines begin
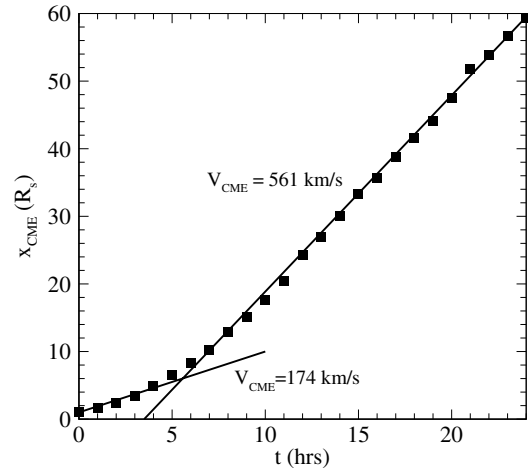

Figure 1. Position of the leading edge of the density-driven CME in the plane of the current sheet as a function of time.

disconnecting from the solar surface resulting in the reformation of the current sheet near the Sun. The solution at $t = 24$ hours in the bottom right panel of Plate 11 clearly
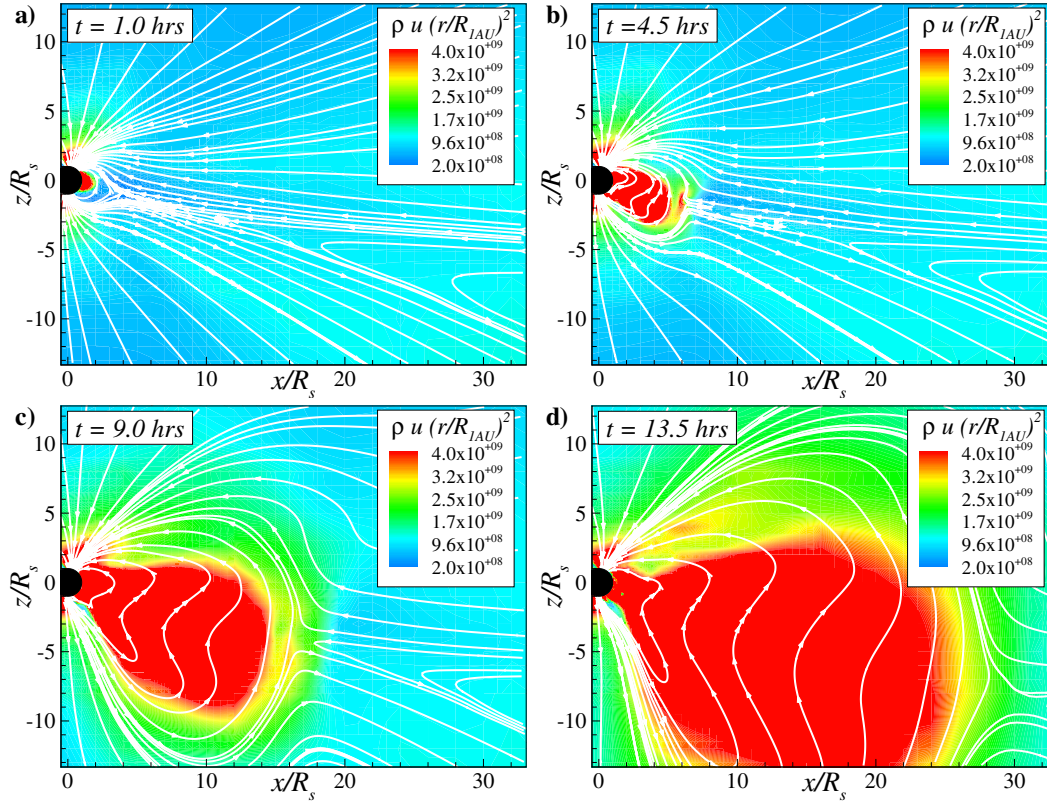
Plate 8. Close-up view of CME evolution in the $y = 0$ meridional plane at (a) $t = 1$ hour, (b) $t = 4.5$ hours, (c) $t = 9$ hours, and (d) $t = 13.5$ hours. Solid white lines are magnetic "streamlines" drawn in the $y = 0$ plane.

depicts this reformation process. Another interesting feature of this simulated space weather event is revealed by the results of Plates 10 and 11, that is, the anisotropic nature of the CME expansion process. As the CME expands in the latitudinal directions, it interacts with higher-speed solar wind and thereby becomes more elongated when viewed in the meridional plane. Refer to Plate 10. Furthermore, the solutions at $t = 12$, 24, and 36 hours indicate that as the CME expands, it remains more concentrated in the latitudinal direction near the disrupted heliospheric current sheet, while spreading much more broadly in the equatorial plane. In fact, it would seem that the circumferential extent of the CME is nearly 360° at $t = 24$ hours, whereas the extent of the CME in the meridional plane is only about 75°–85° in latitude.

4.4. Interaction With the Magnetosphere

The dynamic response of the magnetosphere to the changing solar wind conditions produced by the density-driven CME was also computed as part of the space weather

event simulation. Plate 12 shows the time evolution of the simulated solar wind parameters as would be observed by a monitoring spacecraft located just upstream of the sub-solar terrestrial bow shock. The thin solid lines shown in the graphs represent the variations in the solar wind plasma properties without the CME (these variations are due solely to the solar rotation and spiral nature of the solar wind), while the thick solid lines represent the variations of the free streaming solar wind during the passage of the CME. The coordinate system used in the magnetosphere model is geocentric and moving with the orbiting Earth. A Geocentric Solar Magnetospheric (GSM) coordinate system is adopted with the x axis pointing toward the Sun, the z axis pointing North (perpendicular to the Sun-Earth direction and aligned with the magnetic axis of Earth), and the y axis completing this right-handed coordinate system. When the CME is initiated, Earth is approaching the heliospheric current sheet, and, without the CME, the B_z component of the magnetic field would change sign and remain quite small (<1 nT).

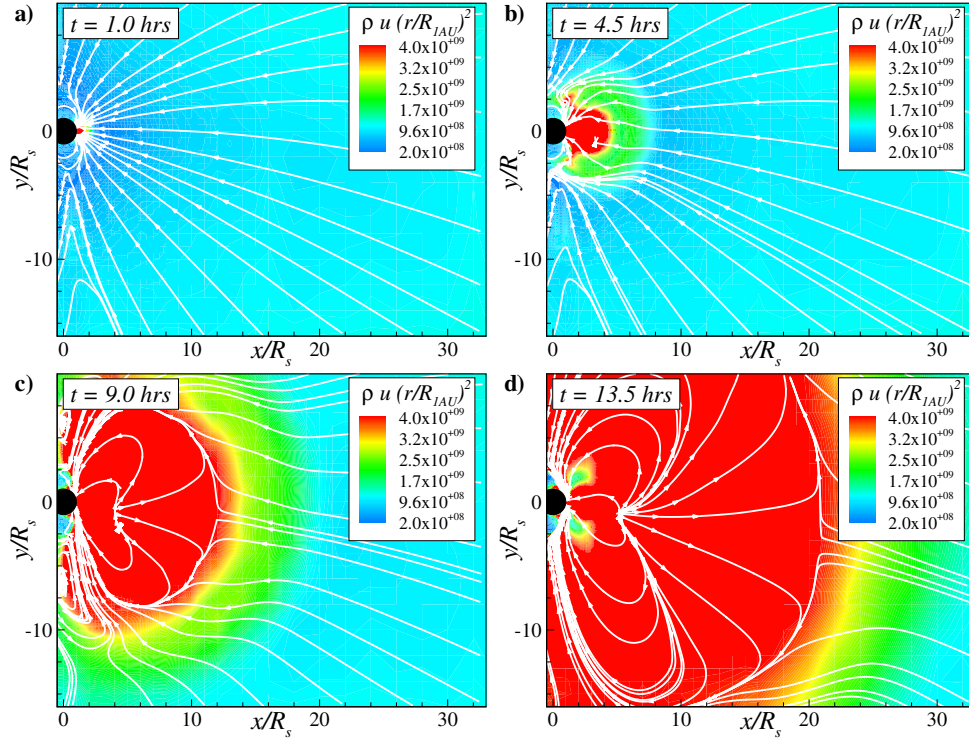Inspection of Plate 12 reveals several interesting features

Plate 9. Close-up view of CME evolution in the equatorial plane at (a) $t = 1$ hour, (b) $t = 4.5$ hours, (c) $t = 9$ hours, and (d) $t = 13.5$ hours. Solid white lines are magnetic "streamlines" drawn in the $z = 0$ plane.

of the solar wind variation produced by the density-driven CME. First of all, the first signatures of the CME can be seen in the magnetic field components at a time somewhere around 54 hours after initiation. The driving mass of the CME (analogous to a piston) arrives after that, around 72 hours after onset. This arrival is indicated by the rapid increase in the solar wind number density starting at $t = 72$ hours. The B_y component of the IMF remains rather steady during the entire event, with its value changing by $<\sim0.5$ nT. The B_x and B_z components of the IMF exhibit somewhat greater changes and indicate that the magnetic field undergoes a significant rotation around the y axis. This, in effect, is the signature of the passage of CME-related magnetic cloud and flux rope. Observations indicate that magnetic clouds are characterized by magnetic fields that smoothly rotate from either north-to-south or south-to-north over a period of ~1 day at 1 AU [*Burlaga et al.*, 1990]. During the simulated CME event the magnitude of the IMF increases from ~2 nT to ~4 nT.

The plasma temperature ($T = T_e + T_p$) of the background steady state solar wind is about 2×10^5 K. During the passage of the CME (beginning at around 55 hours) the plasma temperature decreases rather significantly to values below 1.5×10^5 K. The solar wind velocity remains nearly radial during the entire event with the speed gradually decreasing from ~550 km/s to ~450 km s^{-1}. The undisturbed solar wind density is fairly high prior to the CME event (~35 cm^{-3}), but it decreases to a more typical value of ~18 cm^{-3} before the arrival of the CME driving mass at $t = 72$ hours. At the peak of the simulated event the density increases to ~45 cm^{-3}. The solar wind dynamic pressure (not shown in Plate 12) doubles from its pre-CME value of 2.25 nP (at $t = 72$ hours) to 4.6 nP at the peak of the event.

Plate 13 depicts the changes in global 3-D configuration of the magnetosphere produced by the passage of the CME. Plate 13 shows the magnetospheric solution at two instances in time: $t = 70.5$ hours and 94.5 hours. The color shading represents the electric current density, $\tilde{\mathbf{j}} = \tilde{\nabla} \times \tilde{\mathbf{B}}$, in the terrestrial equatorial plane, and the solid lines represent the last closed magnetic field lines. The field lines on the dayside of the magnetosphere (magnetopause) are shown in green, and the field lines closing in the tail are shown in red. The magnetopause or Chapman-Ferraro current system near the subsolar magnetopause and the cross tail current system
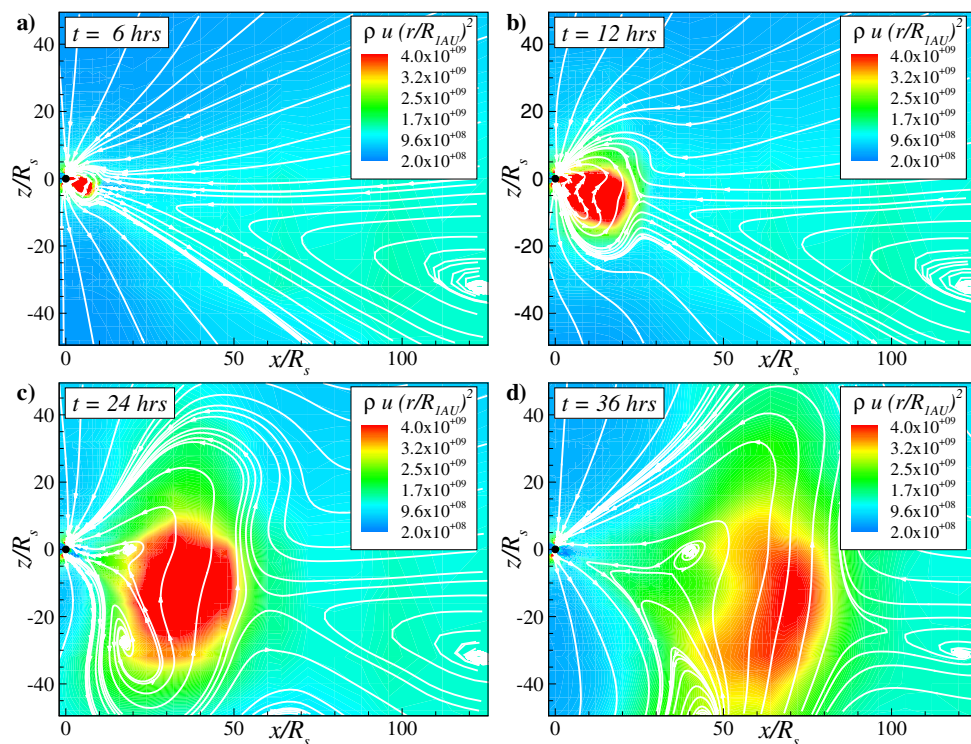
Plate 10. Full view of CME evolution in the $y = 0$ meridional plane at (a) $t = 6$ hours, (b) $t = 12$ hours, (c) $t = 24$ hours, and (d) $t = 36$ hours. Solid white lines are magnetic "streamlines" drawn in the $y = 0$ plane.

on the nightside of the magnetosphere are clearly evident in both solution snapshots.

It is well established that the configuration of the magnetosphere is primarily controlled by the B_z component of the IMF. For $B_z < 0$, observations (confirmed by numerical simulations) indicate that the magnetosphere exhibits an open configuration with significant dayside reconnection and open magnetic field lines connected to large regions near the magnetic poles. For strong northward IMF conditions ($B_z > 5$ nT) the magnetosphere becomes practically closed with magnetic reconnection limited to small regions near the cusps. For "intermediate" values of B_z ($0 < B_z < 5$ nT), numerical simulations performed by the authors indicate that the global magnetospheric configuration is "partially closed" (or "partially open"). In this case, the magnetosphere can be characterized by significant dayside reconnection and large open cusps, by a narrow near-Earth neutral line near the center of the magnetotail (the length of this reconnection line decreases with increasing B_z), and by long, stretched magnetospheric wings connected to the dawnside and duskside of the ionosphere. These wings are formed by highly stretched, closed magnetic field lines and represent the tran-

sition from magnetopause reconnection to tail reconnection (P. Song et al., manuscript in preparation, 2000).

An inspection of Plate 13 reveals that the magnetospheric solutions at $t = 70.5$ hours and 94.5 hours both correspond to the intermediate configuration described above. Furthermore, no significant geomagnetic activity is generated by the interplanetary transient. In the simulated CME event, B_z remains northward for the entire computation, varying between about 0 and 3 nT. The magnetosphere therefore never establishes a configuration that corresponds to either the pure "south" (open) or "north" (closed) configurations but instead exhibits the characteristics of the partially open intermediate configuration for the entire simulation. Furthermore, as the IMF does not switch from northward to southward directions during the simulation (or vice versa), the magnetosphere does not dynamically change from closed to open configurations. A strong southward turning of the IMF is known to trigger substorm activity and result in the formation and release of a plasmoid in the tail of magnetosphere. Furthermore, observations have shown that the energy input to the magnetosphere from any solar wind disturbance depends directly on the strength and duration of southward
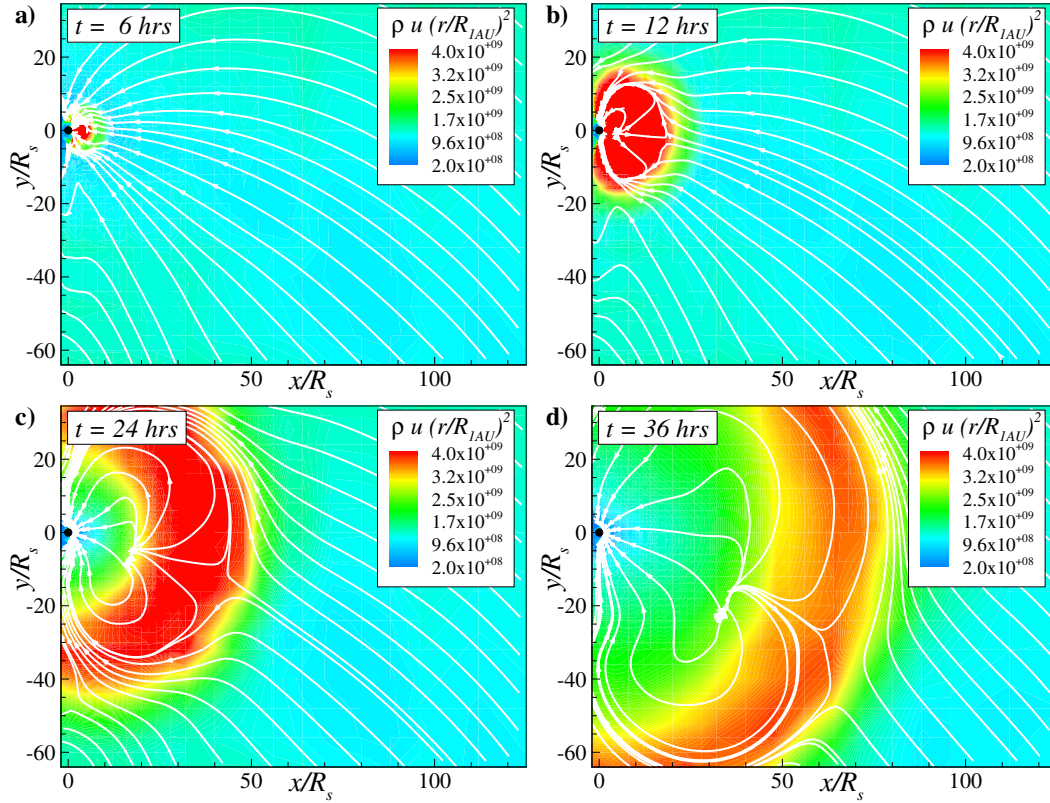
Plate 11. Full view of CME evolution in the equatorial plane at (a) $t = 6$ hours, (b) $t = 12$ hours, (c) $t = 24$ hours, and (d) $t = 36$ hours. Solid white lines are magnetic "streamlines" drawn in the $z = 0$ plane.

IMF [*Russell et al.*, 1974; *Gonzalez et al.*, 1996] and that major magnetic storms are well correlated with strong southward IMF [*Farrugia et al.*, 1997]. As a result, the simulated CME does not produce "dramatic" changes in the computed magnetosphere and would not be classified as a very geoeffective space weather event. Note that an interesting feature of the partially open magnetospheric configurations shown in Plate 13 is the clockwise "twist" of the magnetospheres perpendicular to the solar wind direction. This twist, which is particularly visible in the wings, is due to the presence of a nonzero B_y component in the IMF.

It is felt that the lack of a strong northward to southward turning of the IMF and the lack of a strong southward IMF for any significant period of time are the primary reasons that the simulated CME event produces a relatively "mild" magnetospheric response. The mild response is also partially due to the fact that grid resolution for the solar wind solution is limited at Earth and any solution discontinuities or large solution gradients associated with the CME are somewhat "smeared." It is also believed that the IMF

signature of the simulated CME is a direct consequence of the fact that no emerging magnetic flux was included in the CME initiation process. This is an important limitation of the present model that will be rectified in follow-up studies. Even though the CME did not result in significant geomagnetic activity, the magnetosphere does undergo some important changes during the course of the simulated event. The magnetosphere becomes more compressed because of the passage of the CME. As the solar wind dynamic pressure increases and more than doubles, the bow shock and dayside magnetopause move inward and the magnetospheric current densities significantly increase. In addition, the magnetosphere becomes narrower and magnetospheric wings become longer. The length of the wings increases from about 60 R_e to 90 R_e. Compare the two solutions at $t = 70.5$ hours and 94.5 hours shown in Plate 13. In general, the energy and magnetic flux stored in the magnetosphere can be seen to increase substantially.

Further evidence of the changes in the magnetosphere and ionosphere system produced by the density-driven CME is
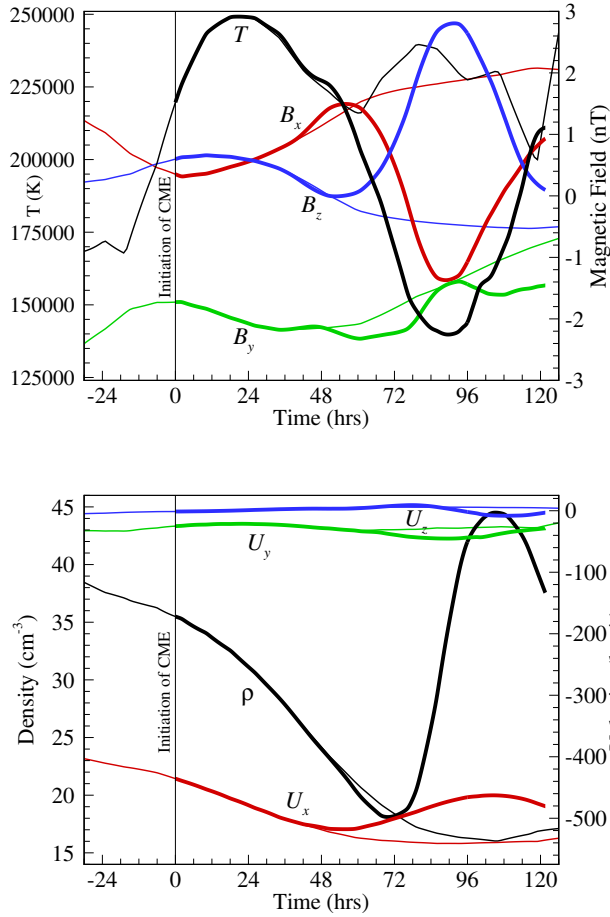
Plate 12. Predicted solar wind plasma parameters at Earth. Thin solid lines represent the steady state solar wind solution without the CME, and thick solid lines represent the solution at Earth when the CME is introduced.

Plate 13. Response of the magnetosphere to the CME. The predicted magnetospheric solution is shown at (top) $t = 70.5$ hours and (bottom) $t = 94.5$ hours. The red and green solid lines represent the last closed magnetic field lines, and the color shading represents current density, $\mathbf{j} = \nabla \times \mathbf{B}$, in the terrestrial equatorial plane.

given Plate 14, which provides polar plots of the ionospheric convection patterns and potential distributions in the ionosphere of the northern hemisphere at $t = 70.5$ and 97.3 hours. The color shading represents the calculated height-integrated ionospheric potential, and the solid white lines represent the predicted convection patterns. Comparison of the two solutions reveals the changes undergone by ionosphere during the CME event. Both solutions exhibit the classic two-cell convection pattern typical of southward-type IMF conditions, and the convection patterns are "twisted" due to the presence of a nonzero B_y component in the IMF. The most important change in the ionosphere is the doubling of the cross-cap potential drop from 30 kV at $t = 70.5$ hours to 60 kV over the 27-hour period of the computation.
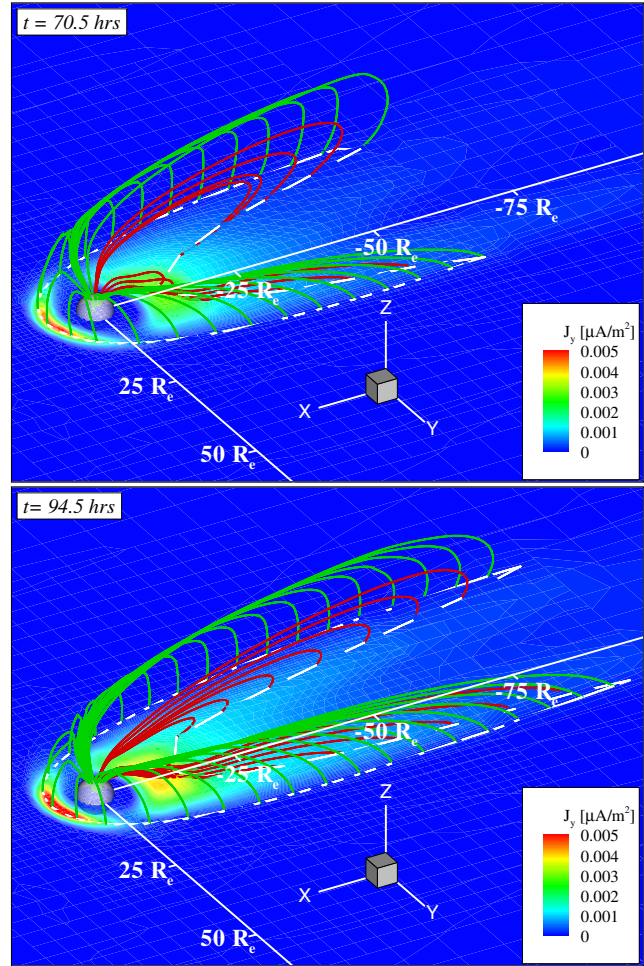
5. Summary and Concluding Remarks

The feasibility of using a parallel AMR scheme that solves the three-dimensional ideal MHD equations to study space weather events and their impact on Earth has been investigated. A newly developed global 3-D MHD model has been used to simulate the initiation, structure, and evolution of a density-driven CME propagating from the solar surface out to distances beyond 1 AU. The subsequent interaction of this solar wind disturbance with the terrestrial magnetosphere has also been predicted. As part of this work, a steady state solution for solar wind has also been devel-
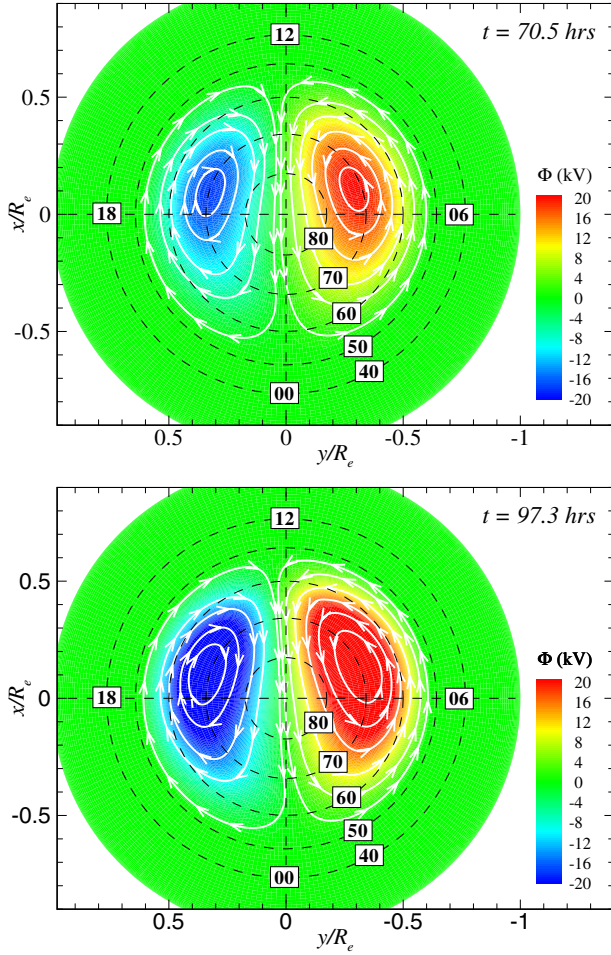
Plate 14. Polar plots of the ionospheric convection (solid white lines) and potential distribution (color shading) in the ionosphere of the northern hemisphere at (top) $t = 70.5$ hours and (bottom) $t = 97.3$ hours.

oped and presented that is in good overall agreement with the average observed solar wind features. Although it was predicted that the simulated CME event would not lead to significant geomagnetic activity at Earth, the numerical results represent the first simulation of a complete fully three-dimensional space weather event and demonstrate the potential of the parallel MHD model for enhancing the understanding of transient solar wind disturbances, space weather phenomena, and hence the coupling that exists between the Sun and Earth systems.

Future research will involve more detailed investigations using more physically realistic mathematical descriptions of the plasma dynamic behavior, solar magnetic field configurations, and initiation mechanisms for CMEs. In particular,

the inclusion of an emerging magnetic flux in the CME initiation process is expected to increase the magnetic signature of the CME at Earth orbit and thus lead to a much more geoeffective event. It is our intention to carry such a simulation in the near future.

Appendix A: Parallel AMR Scheme for MHD

A parallel AMR finite-volume scheme is used to solve the MHD equations outlined in section 2. This solution technique has been formulated to capitalize on recent developments in three areas of scientific computing. They are (1) advances in upwind finite-volume methods for hyperbolic conservation laws; (2) significant advances in solution-adaptive techniques; and (3) advances in parallel computer design. A reliable, relatively efficient, and scalable method for solving the MHD equations has resulted. Although aspects of the solution algorithm are described elsewhere [*Powell et al.*, 1999; *Groth et al.*, 1999], the first detailed description of the algorithm for simulating space weather events, including the parallel implementation, is provided in this appendix for the sake of completeness.

A1. Symmetrizable Form of MHD Equations

The hyperbolic system of partial differential equations (PDEs) given by (1)–(4) can be re-expressed in weak conservation (divergence) form as

$$\frac{\partial \tilde{\mathbf{U}}}{\partial \tilde{t}} + \left(\tilde{\nabla} \cdot \tilde{\mathbf{F}} \right)^T = \tilde{\mathbf{S}} + \tilde{\mathbf{Q}}, \tag{A1}$$

where the solution and source-like vectors $\tilde{\mathbf{U}}$ and $\tilde{\mathbf{S}}$ are given by

$$\tilde{\mathbf{U}} = \begin{bmatrix} \tilde{\rho} \\ \tilde{\rho}\tilde{\mathbf{u}} \\ \tilde{\mathbf{B}} \\ \tilde{E} \end{bmatrix} \qquad \tilde{\mathbf{S}} = - \begin{bmatrix} 0 \\ \tilde{\mathbf{B}} \\ \tilde{\mathbf{u}} \\ \tilde{\mathbf{u}} \cdot \tilde{\mathbf{B}} \end{bmatrix} \tilde{\nabla} \cdot \tilde{\mathbf{B}}, \tag{A2}$$

$\tilde{\mathbf{F}}$ is a flux tensor having the form

$$\tilde{\mathbf{F}} = \begin{bmatrix} \tilde{\rho}\tilde{\mathbf{u}} \\ \tilde{\rho}\tilde{\mathbf{u}}\tilde{\mathbf{u}} + \left(\tilde{p} + \frac{1}{2}\tilde{B}^2 \right) \mathbf{I} - \tilde{\mathbf{B}}\tilde{\mathbf{B}} \\ \tilde{\mathbf{u}}\tilde{\mathbf{B}} - \tilde{\mathbf{B}}\tilde{\mathbf{u}} \\ \tilde{\mathbf{u}}\left(\tilde{E} + \tilde{p} + \frac{1}{2}\tilde{B}^2 \right) - \left(\tilde{\mathbf{B}} \cdot \tilde{\mathbf{u}} \right) \tilde{\mathbf{B}} \end{bmatrix}^T, \tag{A3}$$

and the total plasma energy $\tilde{E}$ is given by

$$\tilde{E} = \frac{1}{2}\tilde{\rho}\tilde{u}^2 + \frac{\tilde{p}}{\gamma - 1} + \frac{1}{2}\tilde{B}^2. \tag{A4}$$

In this formulation the vector $\tilde{\mathbf{S}}$ contains terms arising in the MHD equations that cannot be expressed in divergence form (this issue will be discussed below), and the column vector $\tilde{\mathbf{Q}}$ contains source terms associated with solar gravitational and rotational effects as well as the effects of coronal heating processes and heat and radiation transfer effects. The vector $\tilde{\mathbf{Q}}$ is given by

$$
\tilde{\mathbf{Q}} = \begin{bmatrix} 0 \\ \tilde{\rho}\left[\tilde{\mathbf{g}} - \tilde{\mathbf{\Omega}} \times \left(\tilde{\mathbf{\Omega}} \times \tilde{\mathbf{r}}\right)\right] - 2\tilde{\rho}\tilde{\mathbf{\Omega}} \times \tilde{\mathbf{u}} \\ 0 \\ \tilde{\rho}\tilde{\mathbf{u}} \cdot \left[\tilde{\mathbf{g}} - \tilde{\mathbf{\Omega}} \times \left(\tilde{\mathbf{\Omega}} \times \tilde{\mathbf{r}}\right)\right] + \tilde{\rho}\tilde{q}\left(\tilde{T}_\circ - \gamma\frac{\tilde{p}}{\tilde{\rho}}\right) \end{bmatrix} . \quad (A5)
$$

The form of the MHD equations given by (A1)–(A5) is somewhat nonstandard. The terms of column vector $\tilde{\mathbf{S}}$ are proportional to $\nabla \cdot \tilde{\mathbf{B}}$ and arise solely from expressing Faraday's law in divergence form. It is more usual to make use of the solenoidal condition, $\nabla \cdot \tilde{\mathbf{B}} = 0$, to further simplify (A1). The solenoidal condition amounts to an initial condition for the MHD equations and, physically, implies that there are no magnetic monopoles. However, imposing this constraint in finite-volume-based numerical solutions of the MHD equations has proven to be very challenging [*Brackbill and Barnes*, 1980]. Mathematically, dropping the source terms of $\tilde{\mathbf{S}}$ changes the mathematical properties of the MHD equations. *Godunov* [1961, 1972] has shown that (A1) with the additional constraint is not symmetrizable. The equations possess a degenerate eigensystem, having only seven identifiable characteristic fields and, furthermore, are not formally Galilean invariant. *Godunov* [1961, 1972] found that the MHD equations can only be rendered symmetrizable by retaining the terms contained in $\tilde{\mathbf{S}}$. Equation (A1) with the source terms of $\tilde{\mathbf{S}}$ has eight characteristic fields, satisfies an additional transport equation or balance law (in addition to the original eight equations) for the plasma entropy, and is Galilean invariant. Moreover, this form of the MHD equations allows the derivation of an eight-wave approximate Roe-type Riemann solver that can be used in the construction of an upwind finite-volume scheme [*Powell*, 1994; *Powell et al.*, 1999].

The approach taken here, as first advocated by *Powell* [1994], is to solve the governing PDEs in their symmetrizable form. This permits the construction of a finite-volume scheme, based on approximate Riemann solvers, that tightly couples the fluid-dynamics and magnetic field equations and thereby correctly represents the propagation speeds of solution disturbances. Although the solenoidal condition is not enforced to machine accuracy, it can be shown that it is satisfied to the level of the truncation error of the solver without requiring the use of projection schemes and/or staggered mesh arrangements [*Tóth and Odstrčil*, 1996; *Powell et al.*, 1999]. Furthermore, *Tóth and Odstrčil* [1996] have found that the addition of the terms proportional to $\nabla \cdot \tilde{\mathbf{B}}$ improves results for multidimensional MHD calculations with several methods and, in fact, reduces errors in the computed parallel magnetic force.

Careful numerical testing of the $\nabla \cdot \tilde{\mathbf{B}}$ error was carried out by *Powell et al.* [1999]. It was shown that the quantity $h\nabla \cdot \mathbf{B}$, where h is the local mesh spacing, decreases with increased grid resolution. Since the quantity $h\nabla \cdot \mathbf{B}$ is the quantity that actually enters in the update equations, the overall numerical error of the scheme, even directly in the vicinity of shocks, decreases with increasing resolution. In smooth flow regions, $\nabla \cdot \mathbf{B}$ itself decreases with increasing resolution and so in these regions the numerical error decreases even more rapidly with increased mesh resolution. The truncation-error-level values of $\nabla \cdot \mathbf{B}$ that occur in shocks do not affect the magnetic topology of the flows or the overall second-order nature of the numerical scheme. It was also shown that errors in all primitive quantities, including magnetic field, decreased with the square of the mesh size in smooth regions and linearly with the mesh size in discontinuous regions.

A2. Finite-Volume Scheme

In the present work, an explicit higher-order Godunov-type method is used to solve (A1). In this finite-volume approach the governing equations are integrated over a computational cell i, yielding

$$
\frac{d\tilde{\mathbf{U}}_i}{d\tilde{t}} = -\frac{1}{V_i}\sum_{\text{faces}}\tilde{\mathbf{F}} \cdot \mathbf{n}A - \frac{\tilde{\mathbf{S}}_i}{V_i}\sum_{\text{faces}}\tilde{\mathbf{B}} \cdot \mathbf{n}A + \tilde{\mathbf{Q}}_i , \quad (A6)
$$

where V_i is the volume of cell i, A is the surface area of the faces forming the computational cell, $\mathbf{n}$ is the unit vector normal to the cell faces, $\tilde{\mathbf{U}}_i$ is the cell-averaged conserved solution vector, and $\tilde{\mathbf{S}}_i$ is given by

$$
\tilde{\mathbf{S}}_i = -\begin{bmatrix} 0 \\ \tilde{\mathbf{B}}_i \\ \tilde{\mathbf{u}}_i \\ \tilde{\mathbf{u}}_i \cdot \tilde{\mathbf{B}}_i \end{bmatrix} . \quad (A7)
$$

The numerical face fluxes, $\tilde{\mathbf{F}} \cdot \mathbf{n}$, are defined in terms of the left and right interface solution states, $\mathbf{U}_\text{L}$ and $\mathbf{U}_\text{R}$, as follows

$$
\tilde{\mathbf{F}} \cdot \mathbf{n} = \mathcal{F}\left(\mathbf{U}_\text{L}, \mathbf{U}_\text{R}, \mathbf{n}\right) , \quad (A8)
$$

where $\mathbf{U}_\text{L}$ and $\mathbf{U}_\text{R}$ are determined using piece-wise linear solution reconstruction applied to each computational cell. The least squares limited linear reconstruction procedure developed by *Barth* [1993] is used here. Given the left and

right interface states, the flux function $\mathcal{F}$ is then evaluated by using an approximate Riemann solver. In the present work, the Roe-type linearized Riemann solver for MHD put forward by *Powell* [1994] and *Linde*'s [1998] flux function have both been implemented and may be used. We note that the use of limited linear reconstruction and approximate Riemann solvers leads to a scheme that is robust, minimizes numerical discretization errors, and provides accurate resolution of discontinuities and shocks. Further details of this spatial discretization procedure and the approximate Riemann solvers used here are given elsewhere [*Powell*, 1994; *Powell et al.*, 1995, 1999; *Linde*, 1998].

For steady state calculations a time-marching method-of-lines approach is adopted, and the system of ordinary differential equations resulting from the application of the spatial discretization procedure defined above is integrated in time using the optimally smoothing multistage schemes developed by *van Leer et al.* [1989]. The general M stage scheme for integrating (A6) from time level n to time level $n + 1$ can be written as

$$\tilde{\mathbf{U}}_i^{(0)} = \tilde{\mathbf{U}}_i^n$$
$$\tilde{\mathbf{U}}_i^{(m)} = \tilde{\mathbf{U}}_i^{(0)} + \beta_m \Delta \tilde{t}^n \mathbf{R}\left(\tilde{\mathbf{U}}_i^{(m-1)}\right) \quad m = 1 \ldots M \quad \text{(A9)}$$
$$\tilde{\mathbf{U}}_i^{(n+1)} = \tilde{\mathbf{U}}_i^{(M)}$$

where the residual $\mathbf{R}$ is equal to the right-hand side of (A6) and $\Delta \tilde{t}^n = \tilde{t}^{n+1} - \tilde{t}^n$ is the size of the time step. The multistage coefficients β_m and associated timestep constraints are given by *van Leer et al.* [1989]. One advantage of this integration procedure is its low storage requirement. Local time stepping is used to enhance the convergence of the scheme to the steady state solution. For time-accurate calculations a simple two-stage second-order Runge-Kutta time integration procedure is used to solve (A6).

A3. Block-Based AMR on Cartesian Grids

Adaptive mesh refinement techniques that automatically adapt the computational grid to the solution of the governing PDEs can be very effective in treating problems with disparate length scales. Methods of this type avoid underresolving the solution in regions deemed of interest (e.g., high-gradient regions) and, conversely, avoid overresolving the solution in other less interesting regions (low-gradient regions), thereby saving orders of magnitude in computing resources for many problems. For typical solar wind flows, length scales can range from tens of kilometers in the near Earth region to the Earth-Sun distance (1.5×10^{11} m), and timescales can range from a few seconds near the Sun to the expansion time of the solar wind from the Sun to the Earth ($\sim 10^5$ s). The use of AMR is extremely beneficial and al-
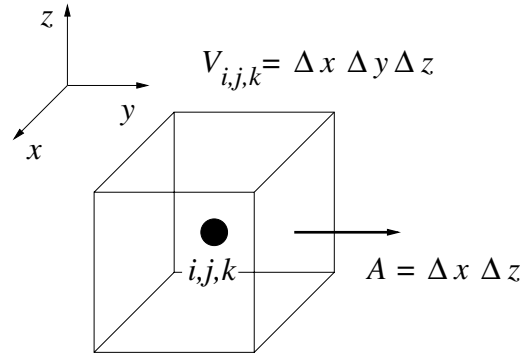

Figure A1. Cartesian computational cell used in parallel block-based AMR scheme.

most a virtual necessity for solving problems with such disparate spatial and temporal scales.

Borrowing from previous work by Berger and coworkers [*Berger*, 1982, 1984; *Berger and Colella*, 1989; *Berger and LeVeque*, 1989; *Berger and Saltzman*, 1994], Quirk [*Quirk*, 1991; *Quirk and Hanebutte*, 1993], and *De Zeeuw and Powell* [1993] and keeping in mind the desire for high performance on massively parallel computer architectures, a relatively simple yet effective block-based AMR technique has been developed and is used in conjunction with the finite-volume scheme described above. The method has some similarities with the block-based approaches described by *Quirk and Hanebutte* [1993] and *Berger and Saltzman* [1994]. Here the governing equations are integrated to obtain volume-averaged solution quantities within rectangular Cartesian computational cells. A representative cell is depicted in the schematic diagram of Figure A1. The computational cells are embedded in regular structured blocks of equal sized cells. The blocks are geometrically self-similar with dimensions $\tilde{\ell}_x \times \tilde{\ell}_y \times \tilde{\ell}_z$ and consist of $N_x \times N_y \times N_z$ cells, where $\tilde{\ell}_x$, $\tilde{\ell}_y$, and $\tilde{\ell}_z$ are the nondimensional lengths of the sides of the rectangular blocks and N_x, N_y, and N_z are even, but not necessarily all equal, integers. Typically, blocks consisting of anywhere between $4 \times 4 \times 4 = 64$ and $12 \times 12 \times 12 = 1728$ cells are used (see Figure A2). Solution data associated with each block are stored in standard indexed array data structures. It is therefore straightforward to obtain solution information from neighboring cells within a block.

Computational grids are then composed of many self-similar blocks. Although each block within a grid has the same data storage requirements, blocks may be of different sizes in terms of the volume of physical space that they occupy. Starting with an initial mesh consisting of blocks of equal size (i.e., equal resolution), adaption is accom-
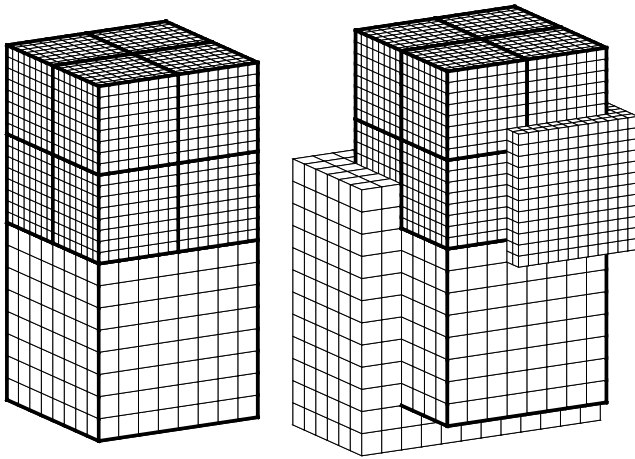
Figure A2. (left) Self-similar blocks used in parallel block-based AMR scheme. (right) Self-similar blocks illustrating the double layer of ghost cells for both coarse and fine blocks.

plished by the dividing and coarsening of appropriate solution blocks. In regions requiring increased cell resolution, a "parent" block is refined by dividing itself into eight "children" or "offspring." Each of the eight octants of a parent block becomes a new block having the same number of cells as the parent and thereby doubling the cell resolution in the region of interest. Conversely, in regions that are deemed overresolved, the refinement process is reversed, and eight children are coarsened and coalesced into a single parent block. In this way, the cell resolution is reduced by a factor of 2. Standard multigrid-type restriction and prolongation operators are used to evaluate the solution on all blocks created by the coarsening and division processes, respectively.

Two neighboring blocks, one of which has been refined and one of which has not, are shown in Figure A2. Any of the blocks shown in Figure A2 can in turn be refined, and so on, leading to successively finer blocks. In the present method, mesh refinement is constrained such that the cell resolution changes by only a factor of 2 between adjacent blocks and such that the minimum resolution is not less than that of the initial mesh.

In order that the update scheme for a given iteration or time step can be applied directly to all blocks in an independent manner, some additional solution information is shared between adjacent blocks having common interfaces. This information is stored in an additional two layers of overlapping "ghost" cells associated with each block as shown in Figure A2. At interfaces between blocks of equal resolution, these ghost cells are simply assigned the solution values associated with the appropriate interior cells of the adjacent
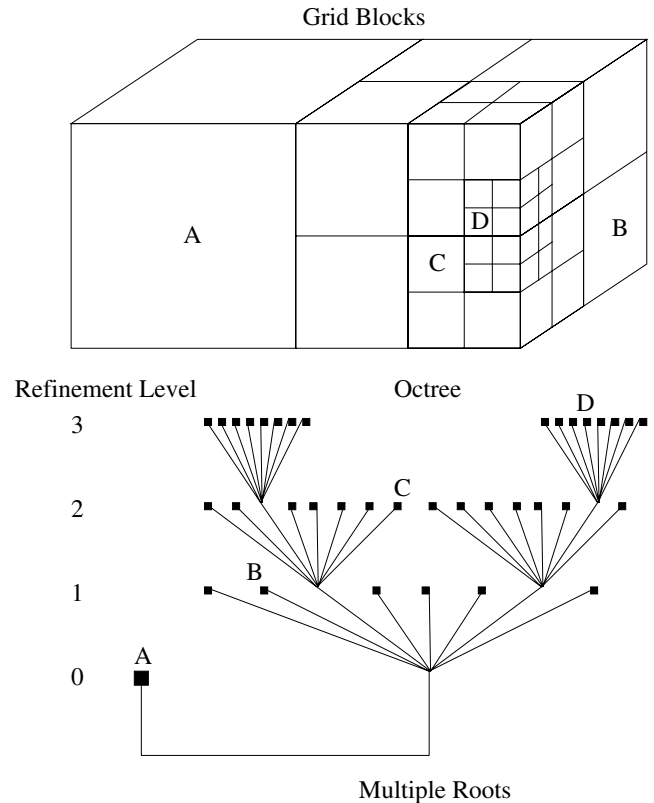

Figure A3. Solution blocks of a computational mesh with three refinement levels originating from two initial blocks and the associated hierarchical multiroot octree data structure. Interconnects to neighbors are not shown.

blocks. At resolution changes, restriction and prolongation operators, similar to those used in block coarsening and division, are employed to evaluate the ghost cell solution values. After each stage of the multistage time-stepping algorithm, ghost cell values are reevaluated to reflect the updated solution values of neighboring blocks. With the AMR approach, additional interblock communication is also required at interfaces with resolution changes to strictly enforce the flux conservation properties of the finite-volume scheme [*Berger*, 1982, 1984; *Berger and Colella*, 1989]. In particular, the interface fluxes computed on more refined blocks are used to correct the interface fluxes computed on coarser neighboring blocks so as to ensure that the fluxes are conserved across block interfaces.

A hierarchical tree-like data structure with multiple "roots," multiple "trees," and additional interconnects between the "leaves" of the trees is used to keep track of mesh refinement and the connectivity between solution blocks. This interconnected "forest" data structure is depicted in

Figure A3. The blocks of the initial mesh are the roots of the forest, which are stored in an indexed array data structure. Associated with each root is a separate "octree" data structure that contains all of the blocks making up the leaves of the tree which were created from the original parent blocks during mesh refinement. Each grid block corresponds to a node of the tree. Traversal of the multitree structure by recursively visiting the parents and children of solution blocks can be used to determine block connectivity. However, in order to reduce overhead associated with accessing solution information from adjacent blocks, the neighbors of each block are computed and stored directly, providing interconnects between blocks in the hierarchical data structure that are neighbors in physical space.

One of the advantages of the preceding hierarchical data structure is that it is relatively easy to carry out local mesh refinement at anytime during a calculation. If, at some point in a computation, a particular region of the flow is deemed to be sufficiently interesting, better resolution of that region can be attained by refining the solution blocks in that region, without affecting the grid structure in other regions of the flow. Reducing the grid resolution in a region is equally easy. There is no need for completely remeshing the entire grid and recalculating block connectivity every time a mesh refinement is performed. Although other approaches are possible, for this study the coarsening and division of blocks are directed using multiple physics-based refinement criteria [*Paillère et al.*, 1992; *Powell et al.*, 1993, 1999]. In particular, decisions as to when to refine or coarsen blocks are made based on comparisons of the maximum values of various local flow quantities determined in each block to specified refinement threshold values. Three flow quantities or refinement criteria, ϵ_k, are used herein. They have the forms

$$\epsilon_1 \propto \left| \tilde{\nabla} \cdot \tilde{\mathbf{u}} \right| \quad \epsilon_2 \propto \left| \tilde{\nabla} \times \tilde{\mathbf{u}} \right| \quad \epsilon_3 \propto \left| \tilde{\nabla} \times \tilde{\mathbf{B}} \right| . \quad \text{(A10)}$$

These quantities represent local measures of the compressibility and vorticity of the plasma as well as the electric current density. They have proven to be quite effective in detecting solution features such as shocks, velocity shears, and current systems in the plasma flow and directing the mesh adaption to more accurately resolve such features. Note that the refinement thresholds are dynamically adjusted so as to exercise some control over the total numbers of blocks, and hence cells, used in a calculation.

An example illustrating the adaptation of the block-based Cartesian mesh to an evolving solution is shown in Figure A4, which shows the grid at four different instances in time for an unsteady calculation and depicts both the solution blocks (thick lines) and computational cells (thin lines) of the evolving grid. As noted above, each level of refinement in the grid introduces cells that are smaller by a fac-

tor 2 in each dimension from those one level higher in the grid. Typically, calculations may have 10-15 levels of refinement; some calculations may have more than 20 levels of refinement. In the case of 20 levels of refinement, the finest cells on the mesh are more than one million times (2^{20}) smaller in each dimension than the coarsest cells. The block-based AMR approach described above has many similarities to the cell-based method proposed by *De Zeeuw and Powell* [1993]. Although the block-based approach is somewhat less flexible and incurs some inefficiencies in solution resolution as compared to a cell-based approach, the block-based method offers many advantages over a cell-based technique when parallel implementations of the algorithms are considered and performance issues are taken into account. As will be discussed below, the block adaptation readily enables domain decomposition and effective load balancing and leads to low communication overhead between solution cells within the same block.

A4. Parallel Implementation

The current and future generations of massively parallel distributed-memory computers offer the potential of large increases in processing power and memory resources beyond those of single-processor machines. Capitalizing on the promise of these resources is, however, not always easily achieved. In many instances, solution algorithm speedup is achieved for small numbers of processors (1–32 processors); however, with added processors, not only does the method fail to scale as expected, but the performance of the algorithm may actually diminish with an increase in the number of processors.

The block-based AMR finite-volume scheme for MHD described in the preceding subsections has been designed with a view to achieving very high performance on massively parallel architectures. In particular, there are several important design features of the method that have enabled high parallel performance. They are as follows:

1. For problems involving the numerical solution of PDEs, domain decomposition (i.e., the partitioning of the problem by dividing the computational domain into subdomains and farming the subdomains off onto separate processors) is a natural and practical approach to parallelization. The hierarchical block-based data structure and self-similar nature of the solution blocks make domain decomposition of the problem almost trivial and readily enable good load balancing, a crucial element for truly scalable computing. Furthermore, the local nature of the mesh refinement process means that mesh adaptation can be performed routinely without remapping all of the subdomains to the processors, which would significantly increase interprocessor communication and reduce computational performance.
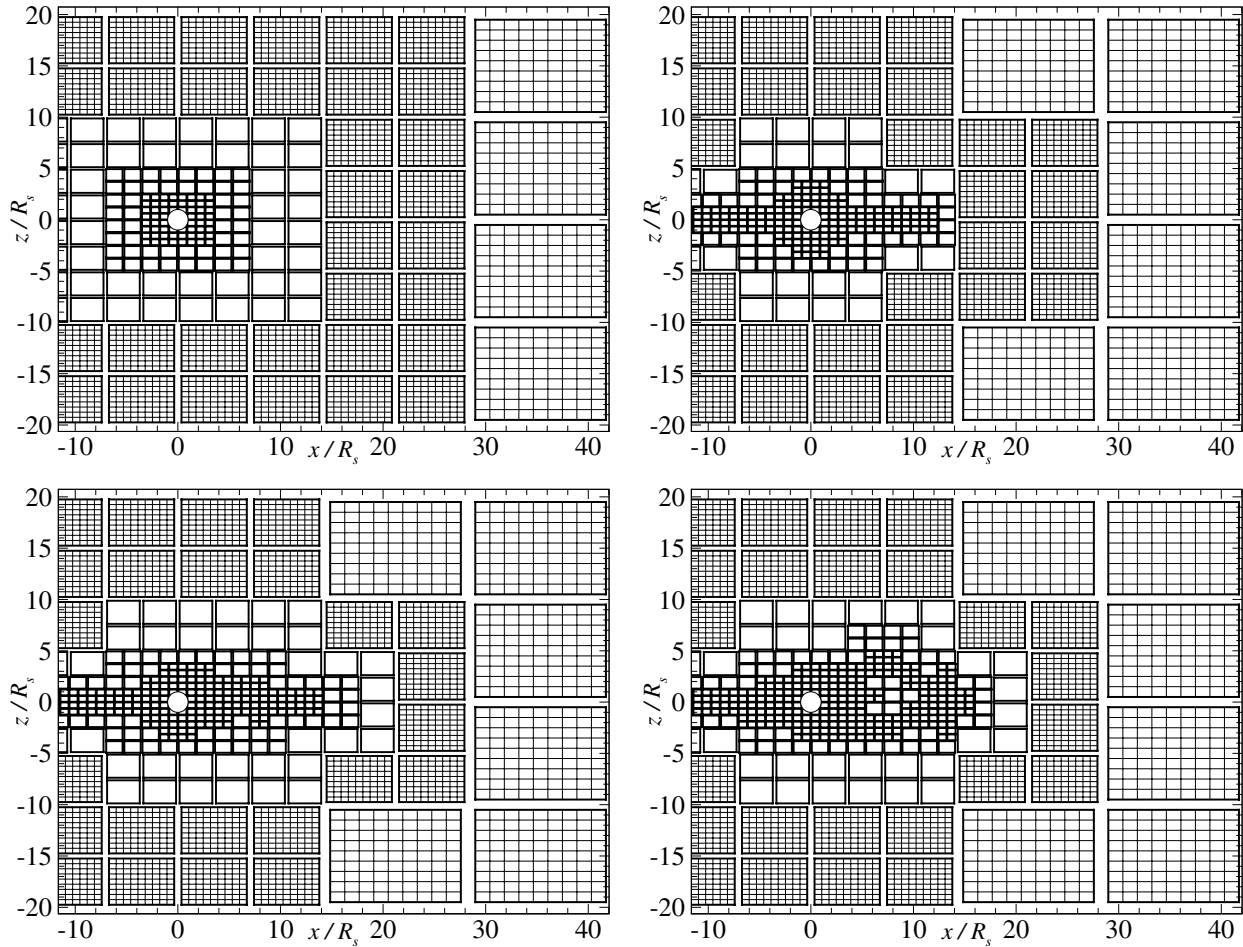
Figure A4. Evolution of a computational mesh illustrating grid adaptation in response to changes in the numerical solution. Cross sectional cuts through a 3-D grid are shown for a solar wind calculation at four different instances in time. The computational cells are not shown for the smaller blocks.

2. Domain decomposition is accomplished by merely farming the solution blocks out to the separate processors, with more than one block permitted on each processor. A simple stack is used to keep track of available (open) processors during refinement and coarsening of the mesh. For homogeneous architectures with multiple processors all of equal speed, an effective load balancing is achieved by exploiting the self-similar nature of the solution blocks and simply distributing the blocks equally amongst the processors. In doing so, all blocks are treated equally, and, currently, no use is made of the hierarchical data structure or grid partitioning techniques to preferentially place neighboring blocks on the same processors. With 10 blocks per processor the load imbalance attained by this simple block distribution procedure is <10% and with 100 blocks per node,

the load imbalance becomes <1%. For heterogeneous parallel machines, such as a network of workstations, a weighted distribution of the blocks can be adopted to preferentially place more blocks on the faster processors and less blocks on the slower processors.

3. The underlying upwind finite-volume solution algorithm, with explicit time stepping, has a very compact stencil and is therefore highly local in nature. This results in lower interprocessor communication requirements. For the block-based grid structure, update of the solution within the subdomains on each processor can proceed almost independently and communication is limited to block interfaces and mainly involves the exchange of ghost-cell solution values and conservative flux corrections. The compact stencil and block

data structure also result in high data locality and therefore permit the more efficient use of processor memory and cache.

4. The self-similar nature of the solution blocks also means that serial performance enhancements apply to all blocks and that fine grain parallelization of the algorithm is possible. In fact, the parallel implementation is such that even much of the grid adaptation can be performed in parallel.

A parallel implementation of the block-based AMR finite-volume scheme has been developed using the FORTRAN 90 programming language and the message passing interface library (MPI). Use of these standards greatly enhances the portability of the computer code and has enabled very good serial and parallel performance. Interprocessor communication is mainly restricted to block interfaces and primarily involves the exchange of ghost-cell solution values and conservative flux corrections. This communication of interface solution information is required at every stage of the multistage solution update procedure. Message passing of the ghost-cell values and flux corrections is performed in an asynchronous fashion with gathered wait states and message consolidation and, as such, typically amounts to only <3-5% of the processor time in most cases.

Implementation of the algorithm has been carried out on SGI and Linux workstations, SGI shared-memory Origin 200 and Origin 2000 machines, a Cray T3D, both Cray T3E-600 and T3E-1200 parallel computers, several IBM SP2 machines, and a few Beowulf clusters. The parallel performance and scalability of the method for several of these architectures are shown in Figures A5 and A6.

Performance results for both Cray T3E-600 and T3E-1200 parallel computers are depicted in Figure A5, which shows two curves for each of these machines: in the first, the performance measured in terms of the number of floating point operations performed per second is shown for a problem that has a fixed number of blocks per processor (the scale-up problem with 16 blocks per processor); in the second, the performance is shown for a problem that has a fixed size of 2,024 blocks (the speed-up problem). Of the two, the second case is more challenging. This is because as the speed-up problem is distributed across more and more processors, the ratio of communication overhead to computing cost increases. The benefits of the bottom-up design of the parallel solver is clearly demonstrated by the results shown in Figures A5 and A6. For both scale-up and speed-up problems the parallel performance of the block-based AMR scheme is linear and nearly 100% efficient for up to 1,024 processors on both the Cray T3E-600 and T3E-1200. Furthermore, 342 GFlops has been attained on the Cray T3E-1200 for the scale-up problem using 1,490 processors.
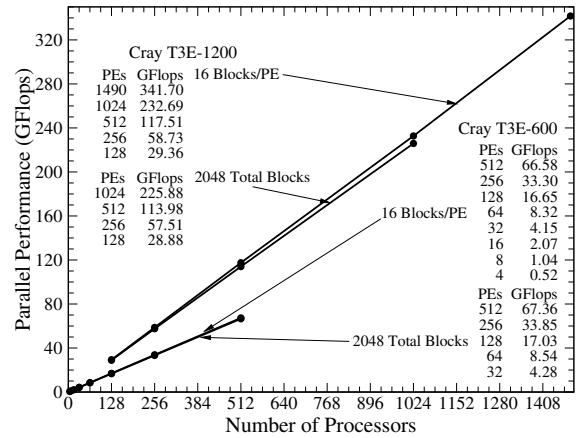

Figure A5. Parallel performance of the block-based AMR scheme for MHD on the Cray T3E-600 and T3E-1200 computers for both scale-up and speed-up problems.
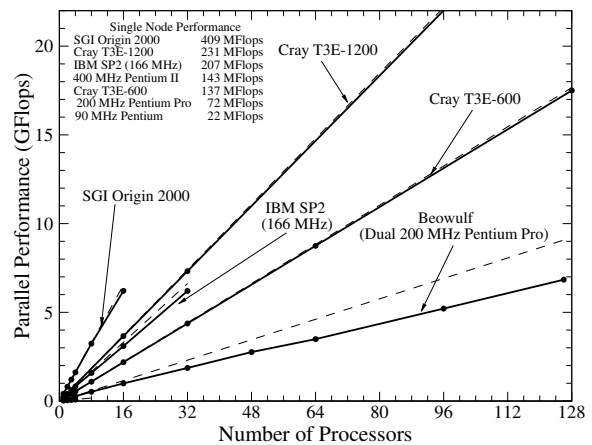

Figure A6. Parallel performance of the block-based AMR scheme for a variety of parallel architectures. The dashed line indicates ideal scale-up performance based on single node performance, and solid lines indicate actual performance achieved on each of the machines for a scale-up problem with 8 blocks per processor.

In Figure A6, the parallel performance obtained on several other architectures is shown and compared to the Cray performance for another scale-up problem with 8 blocks per processor. Although there is generally a higher latency associated with message passing for these other machines, this second set of performance results demonstrates that the block-based algorithm method is portable to a wide range of machines and that reasonable scalability can be achieved,

even for higher-latency architectures such as a Beowulf cluster.

References

Amm, O., Comment on "A three-dimensional, iterative, mapping procedure for the implemention of an ionosphere-magnetosphere anisotropic Ohm's law boundary condition in global magnetohydrodynamic simulations" by Michael L. Goodman, *Ann. Geophys.*, *14*, 773–774, 1996.

Axford, W. I., and J. F. McKenzie, The acceleration of the solar wind, in *Solar Wind Eight*, edited by D. Winterhalter et al., *AIP Conf. Proc. Series*, *382*, 72–75, 1996.

Axford, W. I., and J. F. McKenzie, The solar wind, in *Cosmic Winds and the Heliosphere*, edited by J. R. Jokipii, C. P. Sonett, and M. S. Giampapa, pp. 31–66, Univ. of Ariz. Press, Tucson, 1997.

Barth, T. J., Recent developments in high-order k-exact reconstruction on unstructured meshes, paper presented at *11th AIAA Computational Fluid Dynamics Conference*, Am. Inst. of Aeron. and Astron., Orlando, Fla., 1993.

Berger, M. J., Adaptive mesh refinement for hyperbolic partial differential equations, Ph.D. thesis, Stanford Univ., Stanford, Calif., 1982.

Berger, M. J., Adaptive mesh refinement for hyperbolic partial differential equations, *J. Comput. Phys.*, *53*, 484–512, 1984.

Berger, M. J., and P. Colella, Local adaptive mesh refinement for shock hydrodynamics, *J. Comput. Phys.*, *82*, 67–84, 1989.

Berger, M. J., and R. J. LeVeque, An adaptive Cartesian mesh algorithm for the Euler equations in arbitrary geometries, paper presented at *9th AIAA Computational Fluid Dynamics Conference*, Am. Inst. of Aeron. and Astron., Buffalo, N. Y., 1989.

Berger, M. J., and S. Saltzman, AMR on the CME-2, *Appl. Numer. Math.*, *14*, 239–253, 1994.

Brackbill, J., and D. Barnes, The effect of nonzero $\nabla \cdot \mathbf{B}$ on the numerical solution of the magnetohydrodynamic equations, *J. Comput. Phys.*, *35*, 426–430, 1980.

Brecht, S., J. Lyon, J. Fedder, and K. Hain, A simulation study of east-west IMF effects on the magnetosphere, *Geophys. Res. Lett.*, *8*, 397–400, 1981.

Brecht, S., J. Lyon, J. Fedder, and K. Hain, A time-dependent three-dimensional simulation of the earth's magnetosphere: Reconnection events, *J. Geophys. Res.*, *87*, 6098–6108, 1982.

Burlaga, L. F., R. Lepping, and J. Jones, Global configuraton of a magnetic cloud, in *Physics of Magnetic Flux Ropes*, *Geophys. Monog. Ser.*, vol. 58, edited by C. T. Russell, E. R. Priest, and L. C. Lee, pp. 373–377, AGU, Washington, D. C., 1990.

Chen, J., et al., Evidence of an erupting magnetic flux rope: LASCO coronal mass ejection of 1997 April 13, *Astrophys. J.*, *490*, L191–L194, 1997.

De Zeeuw, D. L., and K. G. Powell, An adaptively-refined Cartesian mesh solver for the Euler equations, *J. Comput. Phys.*, *104*, 55–68, 1993.

Dryer, M., Multidimensional, magnetohydrodynamic simulation of solar-generated disturbances: Space weather forecasting of geomagnetic storms, *AIAA J.*, *3*, 365–370, 1998.

Dryer, M., S. Wu, R. S. Steinolfson, and R. M. Wilson, Magnetohydrodynamic models of coronal transients in the meridional plane, II, Simulation of the coronal transient of 1973 August 21, *Astrophys. J.*, *227*, 1059–1079, 1979.

Farrugia, C. J., L. F. Burlaga, and R. P. Lepping, Magnetic clouds and the quiet-storm effect at Earth, in *Magnetic Storms*, edited by B. T. Tsurutani et al., *Geophys. Monog. Ser.*, vol. 98, pp. 91–106, AGU, Washington, D. C., 1997.

Fedder, J. A., and J. G. Lyon, The solar wind-magnetosphere-ionosphere current-voltage, *Geophys. Res. Lett.*, *14*, 880–883, 1987.

Fedder, J. A., and J. G. Lyon, The Earth's magnetosphere is 165 R_e long: Self-consistent currents, convection, magnetospheric structure, and processes for northward interplanetary magnetic field, *J. Geophys. Res.*, *100*, 3623–3635, 1995.

Fedder, J. A., J. G. Lyon, S. P. Slinker, and C. M. Mobarry, Topological structure of the magnetotail as a function of interplanetary magnetic field direction, *J. Geophys. Res.*, *100*, 3613–3621, 1995a.

Fedder, J. A., S. P. Slinker, J. G. Lyon, and R. D. Elphinstone, Global numerical simulation of the growth phase and the expansion onset for a substorm observed by Viking, *J. Geophys. Res.*, *100*, 19,083–19,093, 1995b.

Fedder, J. A., S. P. Slinker, and J. G. Lyon, A comparison of global numerical simulation results to data for the January 27-28, 1992, Geospace Environment Modeling challange event, *J. Geophys. Res.*, *103*(A7), 14,799–14,810, 1998.

Fisher, R. R., and A. I. Poland, Coronal activity below 2 $R_\odot$: February 15-17, *Astrophys. J.*, *246*, 1004–1009, 1981.

Fisk, L. A., Motion of the footpoints of heliospheric magnetic field lines at the Sun: Implications for recurrent energetic particle events at high heliographic lattitudes, *J. Geophys. Res.*, *101*(A7), 15,547–15,553, 1996.

Fisk, L. A., N. A. Schwadron, and T. H. Zurbuchen, Acceleration of the fast solar wind by the emergence of new magnetic flux, *J. Geophys. Res.*, *104*, 19,765–19,772, 1999a.

Fisk, L. A., T. H. Zurbuchen, and N. A. Schwadron, On the coronal magnetic fields: Consequences of large-scale motions, *Astrophys. J.*, *521*, 868–877, 1999b.

Godunov, S. K., An interesting class of quasilinear systems, *Sov. Math. Dokl.*, *2*, 947–949, 1961.

Godunov, S. K., Symmetric form of the equations of magnetohydrodynamics (in Russian), in *Numerical Methods for Mechanics of Continuum Medium*, vol. 1, pp. 26–34, Siberian Branch of USSR Acad. of Sci., 1972.

Gombosi, T. I., D. L. De Zeeuw, C. P. T. Groth, K. G. Powell, and P. Song, The length of the magnetotail for northward IMF: Results of 3D MHD simulations, in *Physics of Space Plasmas*, vol. 15, edited by T. Chang and J. R. Jasperse, pp. 121–128, MIT Press, Cambridge, Mass., 1998.

Gombosi, T. I., D. L. De Zeeuw, C. P. T. Groth, and K. G. Powell, Magnetospheric configuration for Parker-spiral IMF conditions: Results of a 3D AMR MHD simulation, *Adv. Space Res.*, *26*(1), 139–149, 2000.

Gonzalez, W., B. T. Tsurutani, P. S. McIntosh, and A. L. C. de Gonzalez, Coronal hole–active region–current sheet (CHARCS) association with intense interplanetary and geomagnetic activity, *Geophys. Res. Lett.*, *23*, 2577–2580, 1996.

Goodman, M. L., A three-dimensional, iterative, mapping procedure for the implemenation of an ionosphere-magnetosphere anisotropic Ohm's law boundary condition in global magnetohydrodynamic simulations, *Ann. Geophys.*, *13*, 843–853, 1995.

Groth, C. P. T., D. L. De Zeeuw, K. G. Powell, T. I. Gombosi, and Q. F. Stout, A parallel solution-adaptive scheme for ideal magnetohydrodynamics, paper presented at *14th AIAA Computational Fluid Dynamics Conference*, Am. Inst. of Aeron. and Astron., Norfolk, Va, 1999.

Guo, W. P., and S. T. Wu, A magnetohydrodynamic description of coronal helmet streamers containing a cavity, *Astrophys. J.*, *494*, 419–429, 1998.

Hirayama, T., Theoretical models of flares and prominences, I, Evaporating flare model, *Sol. Phys.*, *34*, 323–338, 1974.

Holzer, T. E., V. H. Hansteen, and E. Leer, Acceleration of the solar wind, in *Cosmic Winds and the Heliosphere*, edited by J. R. Jokipii, C. P. Sonett, and M. S. Giampapa, pp. 239–257, Univ. of Ariz. Press, Tucson, 1997.

Hu, Y. Q., R. Esser, and S. R. Habbal, A fast solar wind model with anisotropic proton temperature, *J. Geophys. Res.*, *102*, 14,661–14,676, 1997.

Hundhausen, A. J., Coronal mass ejections: A summary of SMM observations from 1980 and 1984-1989, in *The Many Faces of the Sun*, edited by K. T. Strong, J. L. R. Soba, and B. M. Haisch, pp. 143–200, Springer-Verlag, New York, 1999.

Illing, R. M. E., and A. J. Hundhausen, Disruption of a coronal streamer by an eruptive prominence and coronal mass ejection, *J. Geophys. Res.*, *91*, 10,951–10,960, 1986.

Janhunen, P., GUMICS-3: A global ionosphere-magnetosphere coupling simulation with high ionospheric resolution, in *Proceedings of the ESA 1996 Symposium on Environment Modelling for Space-Based Applications*, pp. *ESA SP-392*, 233–239, 1996.

Janhunen, P., and H. E. J. Koskinen, The closure of Region-1 field-aligned current in MHD simulation, *Geophys. Res. Lett.*, *24*(11), 1419–1422, 1997.

Kageyama, A., K. Watanabe, and T. Sato, A global simulation of the magnetosphere with a long tail: No interplanetary magnetic field, *J. Geophys. Res.*, *97*, 3929–3943, 1992.

Keppens, R., and J. P. Goedbled, Numerical simulations of stellar winds: Polytropic models, *Astron. Astrophys.*, *343*, 251–260, 1999.

Kopp, R., and G. W. Pneuman, Magnetic reconnection on the corona and the loop prominencce phenomenon, *Sol. Phys.*, *50*, 85–98, 1976.

LeBoeuf, J. N., T. Tajima, C. F. Kennel, and J. M. Dawson, Global simulations of the three-dimensional magnetosphere, *Geophys. Res. Lett.*, *8*, 257–260, 1981.

Linde, T. J., A three-dimensional adaptive multifluid MHD model of the heliosphere, Ph.D. thesis, Univ. of Mich., Ann Arbor, 1998.

Linker, J. A., and Z. Mikić, Disruption of a helmet streamer by photospheric shear, *Astrophys. J.*, *438*, L45–L48, 1995.

Linker, J. A., Z. Mikić, and D. D. Schnack, Modeling coronal evolution, in *Proceedings of the Third SOHO Workshop*, pp. 249–252, Eur. Space Agency, Estes Park, Colo., 1994.

Lionello, R., Z. Mikić, and D. D. Schnack, Magnetohydrodynamics of solar coronal plasmas in cylindrical geometry, *J. Comput. Phys.*, *140*, 172–201, 1998.

Low, B. C., Evolving force-free magnetic fields, I, The development of the preflare stage, *Astrophys. J.*, *212*, 234–242, 1977.

Low, B. C., Eruptive magnetic fields, *Astrophys. J.*, *251*, 352–363, 1981.

Low, B. C., Equilibrium and dynamics of coronal magnetic fields, *Annu. Rev. Astron. Astrophys.*, *28*, 491–524, 1990.

Low, B. C., Magnetohydrodynamic processes in the solar corona: Flares, coronal mass ejections, and magentic helicity, *Plasma Phys.*, *1*, 1684–1690, 1994.

Low, B. C., Solar activity and the corona, *Sol. Phys.*, *167*, 217–265, 1996.

Low, B. C., R. H. Munro, and R. R. Fisher, The initiation of a coronal transient, *Astrophys. J.*, *254*, 335–342, 1982.

Lyon, J. G., J. Fedder, and J. Huba, The effect of different resistivity models on magnetotail dynamics, *J. Geophys. Res.*, *91*, 8057–8064, 1986.

McComas, D. J., et al., Ulysses' return to the slow solar wind, *Geophys. Res. Lett.*, *25*, 1–4, 1998.

Mikić, Z., and J. A. Linker, Disruption of coronal magnetic field arcades, *Astrophys. J.*, *430*, 898–912, 1994.

Mikić, Z., D. Barnes, and D. D. Schnack, Dynamical evolution of a solar coronal magnetic field arcade, *Astrophys. J.*, *328*, 830–847, 1988.

Moore, R. L., D. A. Falconer, J. G. Porter, and S. T. Suess, Coronal heating by magnetic explosions, *Space Sci. Rev.*, *87*, 283–286, 1999.

Neugebauer, M., et al., Spatial structure of the solar wind and comparisons with solar data and models, *J. Geophys. Res.*, *103*, 14,587–14,599, 1998.

Odstrčil, D., and V. J. Pizzo, Distortion of the interplanetary magnetic field by three-dimensional propagation of coronal mass ejections in a structured solar wind, *J. Geophys. Res.*, *104*, 28,225–28,239, 1999a.

Odstrčil, D., and V. J. Pizzo, Three-dimensional propagation of CMEs in a structured solar wind flow, 1, CME launched within the streamer belt, *J. Geophys. Res.*, *104*, 483–492, 1999b.

Odstrčil, D., and V. J. Pizzo, Three-dimensional propagation of coronal mass ejections in a structured solar wind flow, 2, CME launched adjacent to the streamer belt, *J. Geophys. Res.*, *104*, 493–503, 1999c.

Ogino, T., A three-dimensional MHD simulation of the interaction of the solar wind with the Earth's magnetosphere: The generation of field-aligned currents, *J. Geophys. Res.*, *91*, 6791–6806, 1986.

Ogino, T., and R. J. Walker, A magnetohydrodynamic simulation of the bifurcation of tail lobes during intervals with a northward interplanetary magnetic field, *Geophys. Res. Lett.*, *11*, 1018–1021, 1984.

Paillère, H., K. G. Powell, and D. L. De Zeeuw, A wave-model based refinement criterion for adaptive-grid computation of compressible flows, paper presented at 30th Aerosp. Sci. Meet., Am. Inst. of Aeron. and Astron., Reno, Nev., 1992.

Parker, E. N., *Interplanetary Dynamical Processes*, Wiley-Interscience, New York, 1963.

Pneuman, G. W., and R. A. Kopp, Gas-magnetic field interactions in the solar corona, *Sol. Phys.*, *18*, 258–270, 1971.

Powell, K. G., An approximate Riemann solver for magnetohydrodynamics (that works in more than one dimension), *Tech. Rep. 94-24*, Inst. for Comput. Appl. in Sci. and Eng., NASA Langley Space Flight Center, Hampton, Va., 1994.

Powell, K. G., P. L. Roe, and J. Quirk, Adaptive-mesh algorithms for computational fluid dynamics, in *Algorithmic Trends in Computational Fluid Dynmaics*, edited by M. Y. Hussaini, A. Kumar, and M. D. Salas, pp. 303–337, Springer-Verlag, New York, 1993.

Powell, K. G., P. L. Roe, R. S. Myong, T. I. Gombosi, and D. L. DeZeeuw, An upwind scheme for magnetohydrodynamics, paper presented at *12th AIAA Computational Fluid Dynamics Conference*, Am. Inst. of Aeron. and Astron., San Diego, Calif., 1995.

Powell, K. G., P. L. Roe, T. J. Linde, T. I. Gombosi, and D. L. D. Zeeuw, A solution-adaptive upwind scheme for ideal magneto-hydrodynamics, *J. Comput. Phys.*, *154*(2), 284–309, 1999.

Quirk, J. J., An adaptive grid algorithm for computational shock hydrodynamics, Ph.D. thesis, Cranfield Inst. of Technol., Cranfield, England, 1991.

Quirk, J. J., and U. R. Hanebutte, A parallel adaptive mesh refinement algorithm, *Tech. Rep. 93-63*, Inst. for Comput. Appl. in Sci. and Eng., NASA Langley Space Flight Center, Hampton, Va., 1993.

Raeder, J., R. J. Walker, and M. Ashour-Abdalla, The structure of the distant geomagnetic tail during long periods of northward IMF, *Geophys. Res. Lett.*, *22*, 349–352, 1995.

Raeder, J., J. Berchem, M. Ashour-Abdalla, L. A. Frank, W. R. Paterson, K. L. Ackerson, S. Kokubun, T. Yamamoto, and J. A. Slavin, Boundary layer formation in the magnetotail: Geotail observations and comparisons with a global MHD simulation, *Geophys. Res. Lett.*, *24*, 951–954, 1997.

Raeder, J., J. Berchem, and M. Ashour-Abdalla, The geospace environment modeling grand challenge: Results from a global geospace circulation model, *J. Geophys. Res.*, *103*(A7), 14,787–14,797, 1998.

Rosner, R., W. H. Tucker, and G. S. Vaina, Dynamics of the quiescent solar corona, *Astrophys. J.*, *220*, 643–665, 1978.

Russell, C. T., R. L. McPherron, and R. K. Burton, On the cause of geomagnetic storms, *J. Geophys. Res.*, *79*, 1105–1109, 1974.

Schwadron, N. A., L. A. Fisk, and T. H. Zurbuchen, Elemental fractionation in the slow solar wind, *Astrophys. J.*, *521*, 859–867, 1999.

Schwenn, R., Large-scale structure of the interplanetary medium, in *Physics of the Inner Heliosphere*, vol. 1, *Large-Scale Phenomena*, edited by R. Schwenn and E. Marsch, pp. 99–181, Springer-Verlag, New York, 1990.

Song, P., D. L. De Zeeuw, T. I. Gombosi, C. P. T. Groth, and K. G. Powell, A numerical study of solar wind–magnetosphere interaction for northward IMF, *J. Geophys. Res.*, *104*(A12), 28,361–28,378, 1999.

Steinolfson, R. S., Density and white light brightness in looplike coronal mass ejections: Importance of the pre-event atmosphere, *J. Geophys. Res.*, *93*, 14,261–14,267, 1988.

Steinolfson, R. S., Coronal mass ejection shock fronts containing the two types of intermediate shocks, *J. Geophys. Res.*, *95*, 20,693–20,699, 1990.

Steinolfson, R. S., Three-dimensional structure of coronal mass ejections, *J. Geophys. Res.*, *97*, 10,811–10,824, 1992.

Steinolfson, R. S., Modeling coronal streamers and their eruption, *Space Sci. Rev.*, *70*, 289–294, 1994.

Suess, S. T., A.-H. Wang, and S. T. Wu, Volumetric heating in coronal streamers, *J. Geophys. Res.*, *101*(A9), 19,957–19,966, 1996.

Suess, S. T., A. Wang, S. T. Wu, G. Poletto, and D. J. McComas, A two-fluid, MHD coronal model, *J. Geophys. Res.*, *104*, 12,057–12,074, 1999.

Tanaka, T., Generation mechanisms for magnetosphere-ionosphere current systems deduced from a three-dimensional MHD simulation of the solar wind-magnetosphere-ionosphere coupling process, *J. Geophys. Res.*, *100*(A7), 12,057–12,074, 1995.

Tóth, G., and D. Odstrčil, Comparison of some flux corrected transport and total variation diminishing numerical schemes for hydrodynamic and megnetohydrodynamic problems, *J. Comput. Phys.*, *128*(1), 82–100, 1996.

Tsurutani, B. T., and W. D. Gonzalez, The interplanetary causes of magnetic storms: A review, in *Magnetic Storms*, *Geophys. Monogr. Ser.*, vol. 98, edited by T. Tsurutani et al., pp. 77–89, AGU, Washington, D. C., 1997.

Usadi, A., A. Kageyama, K. Watanabe, and T. Sato, A global simulation of the magnetosphere with a long tail: Southward and northward interplanetary magnetic field, *J. Geophys. Res.*, *98*, 7503–7517, 1993.

van Ballegooijen, A. A., and P. C. H. Martens, Magnetic fields in quiescent prominences, *Astrophys. J.*, *361*, 283–289, 1990.

van Leer, B., C. H. Tai, and K. G. Powell, Design of optimally-smoothing multi-stage schemes for the Euler equations, paper presented at *9th AIAA Computational Fluid Dynamics Conference*, Am. Inst. of Aeron. and Astron., Buffalo, New York, 1989.

Wang, A. H., S. T. Wu, S. T. Suess, and G. Poletto, Numerical modeling of coronal mass ejections based on various pre-event model atmospheres, *Sol. Phys.*, *161*, 365–381, 1995.

Wang, A.-H., S. T. Wu, S. T. Suess, and G. Poletto, Global model of the corona with heat and momentum addition, *J. Geophys. Res.*, *103*, 1913–1922, 1998.

Watanabe, K., and T. Sato, Global simulation of the solar wind-magnetosphere interaction: The importance of its numerical validity, *J. Geophys. Res.*, *95*, 75–88, 1990.

White, W. W., G. L. Siscoe, G. M. Erickson, Z. Kaymaz, N. C. Maynard, K. D. Siebert, B. U. Ö. Sonnerup, and D. R. Weimer, The magnetospheric sash and the cross-tail S, *Geophys. Res. Lett.*, *25*(10), 1605–1608, 1998.

Wright, J. M., National Space Weather Program: The Implementation Plan, *FCM-P31,1997*, Off. Fed. Coord. Meteorol. Serv. Supp. Res., Washington, D. C., 1997.

Wu, C. C., R. Walker, and J. M. Dawson, A three-dimensional MHD model of the Earth's magnetosphere, *Geophys. Res. Lett.*, *8*, 523–526, 1981.

Wu, S. T., and W. P. Guo, A self-consistent numerical magneto-
hydrodynamic (MHD) model of helmet streamer and flux rope
interactions: Initiation and propagation of coronal mass ejec-
tions (CMEs), in *Coronal Mass Ejections*, *Geophys. Monogr.
Ser.*, vol. 99, edited by N. Crooker, J. Joselyn, and J. Feynman,
pp. 83–89, AGU, Washington, D. C., 1997.

Wu, S. T., Y. Q. Hu, Y. Nakagawa, and E. Tandberg-Hanssen, In-
duced mass and wave motions in the lower solar atmosphere, I,
Effects of shear motion on flux tubes, *Astrophys. J.*, *266*, 866–
881, 1983.

D. De Zeeuw and T. Gombosi, Space Physics Research
Laboratory, Department of Atmospheric, Oceanic and Space
Sciences, University of Michigan, Ann Arbor, MI 48109–
2143. (darrens@umich.edu, tamas@umich.edu)

C. Groth, University of Toronto Institute for Aerospace
Studies, 4925 Dufferin Street, Toronto, Ontario, Canada
M3H 5T6. (groth@utias.utoronto.ca)

K. Powell, Department of Aerospace Engineering, Uni-
versity of Michigan, Ann Arbor, MI 48109–2118. (pow-
ell@engin.umich.edu)